Cancer Cell

Article

Lymphatic-localized Treg-mregDC crosstalk limits antigen trafficking and restrains anti-tumor immunity

Graphical abstract

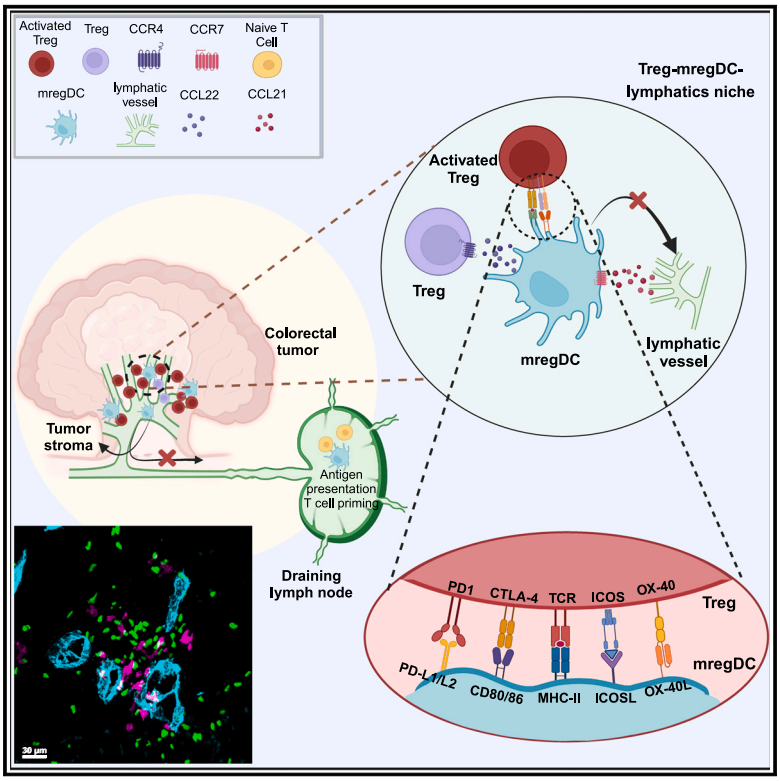

Highlights

- Tregs are especially recruited to peri-lymphatic region in tumor stroma by mregDCs
- The Treg-mregDC-lymphatic niche sustains Treg activation
- Activated Tregs hinder tumor antigen trafficking to dLNs and anti-tumor immunity
- The crosstalk between Tregs and mregDCs predicts worse outcome in human cancers

Authors

Siyuan You, Shuqin Li, Lingsu Zeng, ..., Jiahuai Han, Jianlin Ren, Kairui Mao

Correspondence

maok@xmu.edu.cn

In brief

You et al. show that Tregs are specifically recruited to peri-lymphatic stroma region of colorectal cancer by mregDC forming Treg-mregDC-lymphatic niche, where they acquire activation signature and restrain the trafficking of the tumor antigens to the draining lymph nodes, thereby impeding the initiation of anti-tumor adaptive immune responses.

You et al., 2024, Cancer Cell *42*, 1415–1433
August 12, 2024
https://doi.org/10.1016/j.ccell.2024.06.014

CellPress

Cancer Cell

CellPress

Article

Lymphatic-localized Treg-mregDC crosstalk limits antigen trafficking and restrains anti-tumor immunity

Siyuan You,[1,11] Shuqin Li,[1,11] Lingsu Zeng,[2,3,4,9] Jinsheng Song,[1] Zifeng Li,[1] Weiyun Li,[1,10] Hengxiao Ni,[1] Xu Xiao,[5,6] Wenbo Deng,[7] Hongye Li,[1] Wenbo Lin,[1] Chenyu Liang,[1] Yanfei Zheng,[1] Shih-Chin Cheng,[1,2,8] Nengming Xiao,[1] Mengsha Tong,[1,6] Rongshan Yu,[5,6] Jialiang Huang,[1] Hongling Huang,[1] Hongzhi Xu,[2,3,8] Jiahuai Han,[1] Jianlin Ren,[2,3,8] and Kairui Mao[1,2,8,12,*]

[1]State Key Laboratory of Cellular Stress Biology, Xiang'an Hospital, School of Life Sciences, Faculty of Medicine and Life Sciences, Xiamen University; Xiamen, Fujian 361102, China

[2]Department of Gastroenterology, The National Key Clinical Specialty, Zhongshan Hospital of Xiamen University, School of Medicine, Xiamen University, Xiamen, Fujian 361004, China

[3]Clinical Research Center for Gut Microbiota and Digestive Diseases of Fujian Province, Xiamen Key Laboratory of Intestinal Microbiome and Human Health, Xiamen, Fujian 361004, China

[4]The School of Clinical Medicine, Fujian Medical University, Fuzhou, Fujian 350001, China

[5]School of Informatics, Xiamen University, Xiamen, Fujian 361005, China

[6]National Institute for Data Science in Health and Medicine, Xiamen University, Xiamen, Fujian 361005, China

[7]Key Laboratory of Reproductive Health Research, Fujian Province University, School of Medicine, Xiamen University, Xiamen, Fujian 361102, China

[8]Department of Digestive Diseases, School of Medicine, Xiamen University, Xiamen, Fujian 361102, China

[9]Present address: Department of Gastroenterology, Xiamen Susong Hospital, Xiamen, Fujian, 361100, China

[10]Present address: Cancer Center, Shanghai Tenth People's Hospital, School of Medicine, Tongji University, Shanghai, 200072, China

[11]These authors contributed equally

[12]Lead contact

*Correspondence: maok@xmu.edu.cn

https://doi.org/10.1016/j.ccell.2024.06.014

SUMMARY

The tumor microenvironment (TME) has a significant impact on tumor growth and immunotherapy efficacies. However, the precise cellular interactions and spatial organizations within the TME that drive these effects remain elusive. Using advanced multiplex imaging techniques, we have discovered that regulatory T cells (Tregs) accumulate around lymphatic vessels in the peripheral tumor stroma. This localized accumulation is facilitated by mature dendritic cells enriched in immunoregulatory molecules (mregDCs), which promote chemotaxis of Tregs, establishing a peri-lymphatic Treg-mregDC niche. Within this niche, mregDCs facilitate Treg activation, which in turn restrains the trafficking of tumor antigens to the draining mesenteric lymph nodes, thereby impeding the initiation of anti-tumor adaptive immune responses. Disrupting Treg recruitment to mregDCs inhibits tumor progression. Our study provides valuable insights into the organization of TME and how local crosstalk between lymphoid and myeloid cells suppresses anti-tumor immune responses.

INTRODUCTION

The tumor microenvironment (TME) is composed of proliferating malignant cells, heterogeneous immune cells, diverse fibroblasts, along with vascular and lymphatic endothelial cells and acellular stromal elements.[1] These components dynamically establish a variety of organized micro-structures within the tumor via direct cellular contact as well as paracrine or autocrine communication. Although extensive cataloging of immune and non-immune components in the TME has been conducted using flow cytometry and single cell RNA sequencing,[2–5] and large scale multiplex imaging surveys of mouse and human tumors are beginning to be reported,[6–11] much more information is needed to understand the relationships between the detailed spatial organization of these diverse components and the resulting functional effects on tumor growth or constraint.

Regulatory T cells (Tregs), a specialized T cell lineage expressing the master transcription factor forkhead box protein p3 (Foxp3), play an indispensable role in regulating immune homeostasis and inflammatory responses.[12,13] Meanwhile, their enrichment in the TME also dampens anti-tumor immunity. To restrain self-reactive or anti-tumor immune responses, Tregs utilize a variety of suppressive mechanisms. These mechanisms can be contact-dependent, involving the downregulation of co-stimulatory molecules on dendritic cells (DCs) by CTLA-4, binding of MHC class II with LAG-3, as well as cytolysis of target cells by

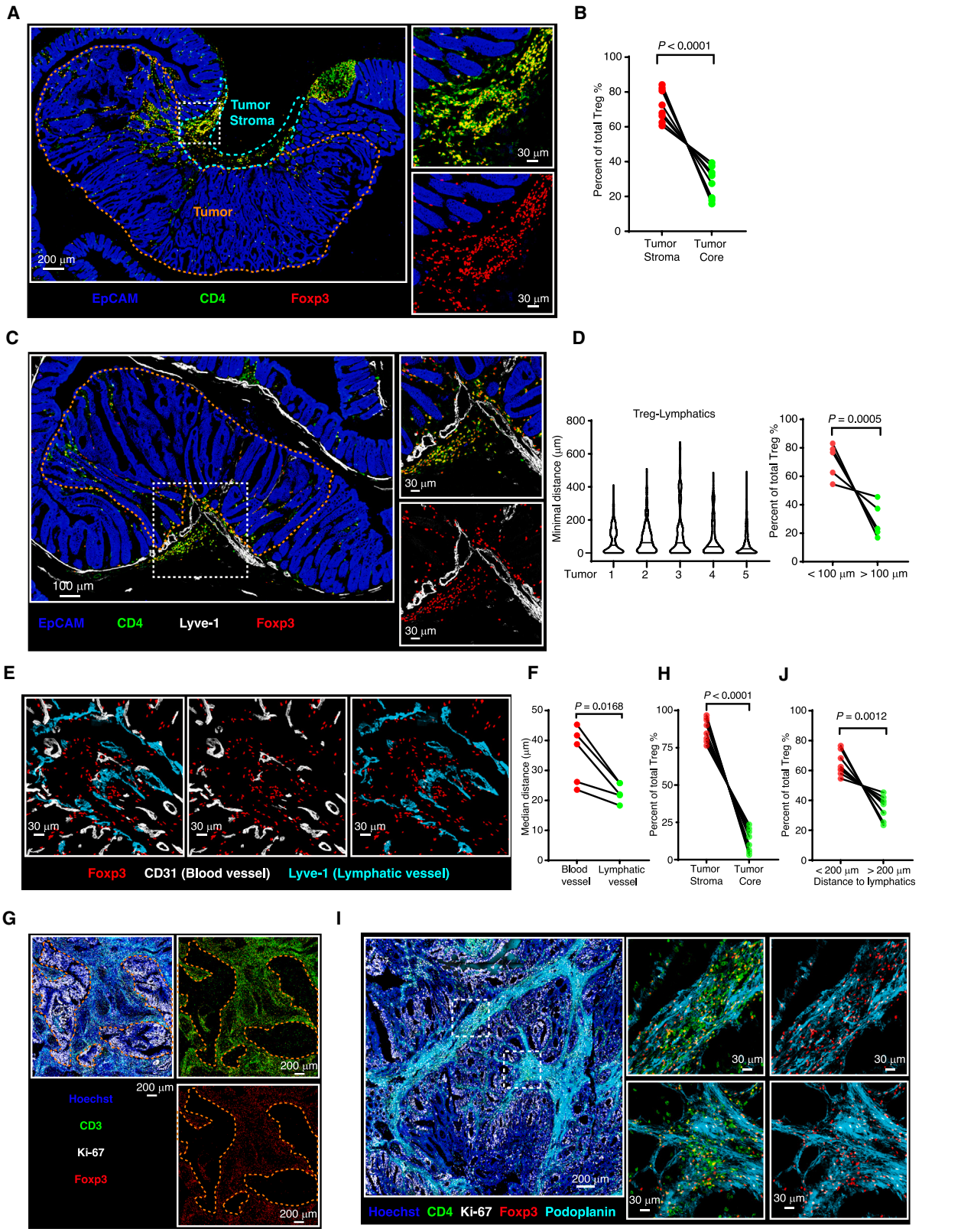

Figure 1. Tregs aggregate in peri-lymphatic regions in mouse and human colorectal cancer

(A and B) Immunofluorescence staining (A) and quantification (B) of Treg distribution in colon tumors from 4-month-old $Apc^{Min/+}$ mice.

(C) Immunofluorescence staining of lymphatic vessels (Lyve-1) and Tregs in colon tumors from $Apc^{Min/+}$ mice.

(legend continued on next page)

granzymes and perforin. Alternatively, they can act in a paracrine-dependent manner, which includes deprivation of IL-2 by CD25, secretion of regulatory cytokines such as IL-10, TGF-β, and IL-35, and conversion of extracellular ATP to adenosine.[13–15] Despite their functional versatility, Tregs deploy distinct mechanisms to act upon target cells in different contexts, depending on their special status and local environment. In secondary lymph tissues, Tregs and self-activated T cells co-localize on migratory DCs bearing self-antigens, where they upregulate effector molecules through TCR and IL-2 signaling to modulate the proliferation and survival of self-activated T cells via a negative feedback loop.[16–19] In cancers, Tregs are not only present in a high proportion but also exhibit an activated state,[20–22] which are associated with worse outcome in patients.[12,23–25] Despite emerging evidence reveals that metabolic cues in TME, such as lactate, play critical roles in Treg proliferation, survival and suppressive functions,[26–29] their spatial distribution, the anatomic niche supporting their activation status and their influence on surrounding cells are largely unknown. A recent study documents that CXCR3 directs Treg's engagement on conventional type 1 dendritic cells (cDC1s) to limit tumor antigen cross-presentation, thus impeding anti-tumor $CD8^+$ T cell response.[30]

A successful anti-tumor immune response relies on a series of events similar to canonical immune responses against pathogens. These events include the uptake and processing of tumor antigens by DCs within tumor, the migration of activated DCs to tumor-draining lymph nodes (tdLNs), the priming of tumor antigen-recognizing T cells, the trafficking of T cells to tumor site and the execution of their effector functions (such as killing tumor cells) upon local re-activation.[31,32] Among these steps, tumor antigen-bearing DCs play a key role in orchestrating T cell priming in draining lymph nodes and reactivation at the tumor site. Extensive evidences have underscored the indispensable roles of conventional DCs, including cDC1s and cDC2s, in orchestrating effective anti-tumor immune responses.[33–37] In addition to cDCs, several studies using single-cell approaches revealed a conserved activated DC state termed mature dendritic cells enriched in immunoregulatory molecules (mregDCs), DC3, or $LAMP3^+$ DC across multiple cancer types in both human and mouse.[5,38–40] These mregDCs express high levels of maturation/activation and migration markers, such as CD80, CD86, CD40, IL-12p40, and CCR7, as well as immunoregulatory signature genes, including PD-L1, PD-L2, and SOCS2. Meanwhile, transcriptomic analysis suggests that mregDCs are potentially developed from both cDC1s and cDC2s, even though they lack cDC1- and cDC2-specific markers.[39,41] Due to their distinct maturation and migration profile, mregDCs are most likely tumor antigen-bearing antigen-presenting cells responsible for initiating and sustaining effective adaptive immune responses, thus associated with favorable prognosis. This is further supported by the findings that mregDCs secret CXCL16 and IL-15 to recruit and maintain the survival of $CD8^+$ T cells in perivascular niches of tumor stroma.[42] However, the crosstalk of mregDC with other immune and non-immune cells in TME, as well as the regulation of their functions by surrounding cells need further investigation.

In this study, we aim to elucidate the distribution of key immune cell populations in the TME, their crosstalk with surrounding cells and the consequent functions in anti-tumor immune response. To investigate these questions in a physiological setting, we utilize a genetically engineered mouse colorectal cancer model ($Apc^{Min/+}$) that is characterized by natural evolution of the TME and close resemblance to human disease.[43–45] Here, we have identified a unique Treg-mregDC-lymphatic niche in tumor stroma. Through interaction with mregDCs, Tregs acquire an activated state and upregulate both suppressive and co-stimulatory surface molecules, which in turn dampen mregDC migration to draining lymph nodes, limiting tumor antigen presentation, and thus hindering the initiation of anti-tumor adaptive immune responses.

RESULTS

Tregs accumulate in the peri-lymphatic region of the tumor stroma

The tumor immune microenvironment, especially the spatial profiling and organization of immune components, plays a crucial role in tumor progression and response to therapy.[46] To examine the detailed organization of tumor immune microenvironment, we employed quantitative multiplex immunohistochemistry (histo-cytometry)[47] to study the distribution of key immune populations in the tumors of $Apc^{Min/+}$ mice, a spontaneous mouse model of colorectal cancer.[43,44] In the normal colon tissue, $Ki67^+$ intestinal epithelial stem cells and transient-amplifying cells are located in crypts, while differentiated epithelial cells lose the capacity to proliferate. However, maturing epithelial cells bearing the *Apc* mutation persistently proliferate and form macroscopic tumors (Figure S1A). The proliferation marker Ki67 allows us to distinguish the tumor from normal tissue and define the tumor margins in this study. We then stained tumor sections with distinct immune cell lineage markers and found that very few $CD8^+$ cytotoxic T cells and B cells infiltrated into the tumor. In contrast, a high frequency of $Foxp3^+$ Tregs specifically aggregated in the stroma of tumor margins, while macrophages and DCs were broadly distributed (Figures 1A, 1B, S1B, and S1C). This specific Treg positioning was also observed in small intestinal tumors (Figure S1D). Consistent with the

(D) Quantification of the minimal distance of Tregs to lymphatic vessels (left panel) and Treg within 100 μm of lymphatics (right panel).
(E and F) Immunofluorescence staining (E) and quantification (F) of the association between Tregs and lymphatic or blood vessels in colon tumors from $Apc^{Min/+}$ mice.
(G and H) Immunofluorescence staining (G) and quantification (H) of Treg distribution in human colorectal tumors.
(I) Immunofluorescence staining of Treg and lymphatic vessels in human colorectal tumors.
(J) Quantification of the Tregs within 200 μm of lymphatics. The dashed orange, cyan, and white lines mark the tumor, tumor stroma and magnified region of interest (ROI), respectively. Images are representative of eight (A, G, and H) and five (C and E) tumors. Each dot represents data from an individual mouse (B, D, and F) or patient (H and J); results are pooled from two (D, F, H, and J) or three (B) independent experiments. Statistical significance was calculated by paired two-tailed Student's t test.
See also Figures S1 and S2 and Video S1.

imaging data, flow cytometry demonstrated the enrichment of Tregs in the tumors compared to lymphoid tissues in $Apc^{Min/+}$ mice (Figure S1E).

Within the stroma of $Apc^{Min/+}$ tumors, Tregs appeared to be concentrated along the vasculature. Staining for lymphatic endothelium revealed that lymphatic vessels protruded into the tumor stroma but not the tumor core as the tumor masses developed. Tregs were visualized along or dispersed around the lymphatic vasculature, with variations in appearance depending on the orientation of the section and tumor size (Figures 1C and S2A). This preferential peri-lymphatic distribution of Tregs was further verified using clearing enhanced 3D (C_e3D)[48] approach at single-cell resolution (Video S1). Quantitative analysis showed that the majority (>70%) of Tregs were within 100 μm of the lymphatics (Figure 1D). In addition to lymphatic vessels, blood vessels are also important components of the tumor vasculature system, providing nutrients, including oxygen, glucose, and growth factors, to tumor cells.[49,50] However, few Tregs aggregated along blood vessels (Figure 1E). Furthermore, quantitative analysis indicated that Tregs positioned much closer to lymphatics than to blood vessels (Figure 1F). The peri-lymphatic location of Tregs in the tumor stroma was not unique to mice. In human colorectal cancer samples, Tregs accumulates in the peri-tumor region where they co-localized with lymphatic vessels, while being limited in number in the tumor core (Figures 1G–1J). Together, these data reveal that Tregs have a unique peri-lymphatic location in both mouse and human colon tumors.

$Apc^{Min/+}$ mice carry a germline mutation that may affect every cell. To determine if the preceding observations were due to a cell-intrinsic effect of the *Apc* mutation in immune cells or other non-epithelial cells, we used $Villin^{Cre}$ $Apc^{fl/+}$ mice.[51] These mice have one copy of the *Apc* allele specifically deleted in intestinal epithelial cells and spontaneously develop intestinal adenomas as $Apc^{Min/+}$ mice. The similar Treg distribution pattern in these epithelial-selective mutant mice indicated that Treg peri-lymphatic distribution arose from the physiology of these cells in the context of the TME rather than the action of the *Apc* gene mutation (Figure S2B). Because the microbiome also plays an important role in shaping the TME, especially in colorectal cancer,[52,53] $Apc^{Min/+}$ mice were treated with broad-spectrum antibiotics to evaluate the contribution of commensal bacteria to the positioning of Tregs. The clearance of the gut microbiota did not influence Treg aggregation around lymphatic vessels (Figure S2C), suggesting that Treg peri-lymphatic location in tumor stroma was driven by the tumor milieu rather than gut microbiota.

To investigate whether Treg aggregation in tumor stroma influenced tumor growth, particularly by suppressing anti-tumor immunity and thereby enhancing tumor progression, we generated $Apc^{Min/+}Foxp3^{DTR}$ mice, which allowed for Treg depletion by administration of diphtheria toxin (DTX). Transient Treg depletion resulted in a significant increase in $CD8^+$ T cell infiltration into the tumor (Figures S2D and S2F). However, prolonged and continuous Treg depletion can lead to severe autoimmunity. Therefore, we applied two rounds of DTX treatment at three-week interval (Figure S2G). This regimen markedly diminished tumor incidence in both the small intestine and colon (Figures S2H and S2I). To further elucidate whether the diminished tumor formation following Treg depletion stemmed from enhanced anti-tumor adaptive immunity, we generated $Apc^{Min/+}Tcra^{-/-}$ mice, which lack both Tregs and conventional $CD4^+$ and $CD8^+$ T cells. The comparable tumor burdens in these mice as $Apc^{Min/+}$ mice suggested that effective anti-tumor adaptive immune responses were necessary for tumor clearance in the absence of Tregs (Figures S2J and S2K). Taken together, these data suggest a tumor-intrinsic mechanism that recruits Tregs to the peri-lymphatic stromal region, which in turn suppresses anti-tumor immunity and facilitates tumor progression.

Transcriptomic analysis reveals correlation between Tregs and mregDCs

The peri-lymphatic distribution of Tregs in tumor stroma raises two important questions: first, why do Tregs aggregate along lymphatic vessels and second, how do Tregs in this specific location suppress anti-tumor immunity? To investigate the mechanisms governing Treg positioning, we examined the transcriptional profile and clonality of tumor Tregs using bulk RNA and TCR sequencing. Compared to their colonic counterparts, tumor Tregs exhibited high expression of 622 genes, including *Pdcd1*, *Tnfrsf9*, *Ctla4*, and *Icos* (Figure S3A). Both Gene Ontology (GO) analysis and gene set enrichment analysis (GSEA) revealed upregulation of T cell activation and cell-cell adhesion genes in tumor-infiltrating Tregs (Figures S3B and S3C), consistent with findings in human tumor-infiltrating Tregs.[20] This highly activated state of tumor Tregs was confirmed at the protein level by flow cytometry, with notable variation in the expression levels of these molecules among Tregs (Figures S3D and S3E). Concurrent with their activated state, TCR repertoire analysis unveiled significantly clonal expansion among tumor-infiltrating Tregs compared to their colonic counterparts (Figures S3F and S3G), suggesting that a subset of Tregs underwent activation and clonal expansion within the TME.

We next isolated total immune cells from colon tissues of wild-type mice and tumors of $Apc^{Min/+}$ mice and performed single-cell RNA sequencing (scRNA-seq) to investigate their state in greater depth. We obtained 23,922 cells with high-quality transcriptomes and identified eight main cell clusters containing B cells, T and innate lymphoid cells (T/ILC), neutrophils, monocytes, macrophages, mast cells, DCs, and an undefined cluster based on canonical markers (Figures 2A and S4A). Compared to colon tissue, neutrophils and monocytes were preferentially enriched in tumor and exhibited characteristics of myeloid-derived suppressor cells (Figures S4B and S4C). Based on the expression of signature genes, the T/ILC cell cluster was further divided into NK cells, ILCs, conventional $CD4^+$ T cells (CD4 Tconv), Tregs, $CD8^+$ T cells, and $CD4^-CD8^-$ double-negative T cells (DN_T) that included γδT cells (Figures 2A and S4D). In agreement with previous flow cytometry findings (Figure S1E), Tregs were specifically recruited into the tumors. Concurrently, NK and ILCs were more abundant in colon tissues, while $CD4^-CD8^-$ DN_T cells were enriched in tumor (Figures S4D and S4E). We then focused on the transcriptome of the tumor Treg population, which was further divided into two states, activated and quiescent, using gene set variation analysis (GSVA),[54] distinguished by the expression levels of T cell activation-associated genes (Figures 2B and S4F). This binary definition of tumor

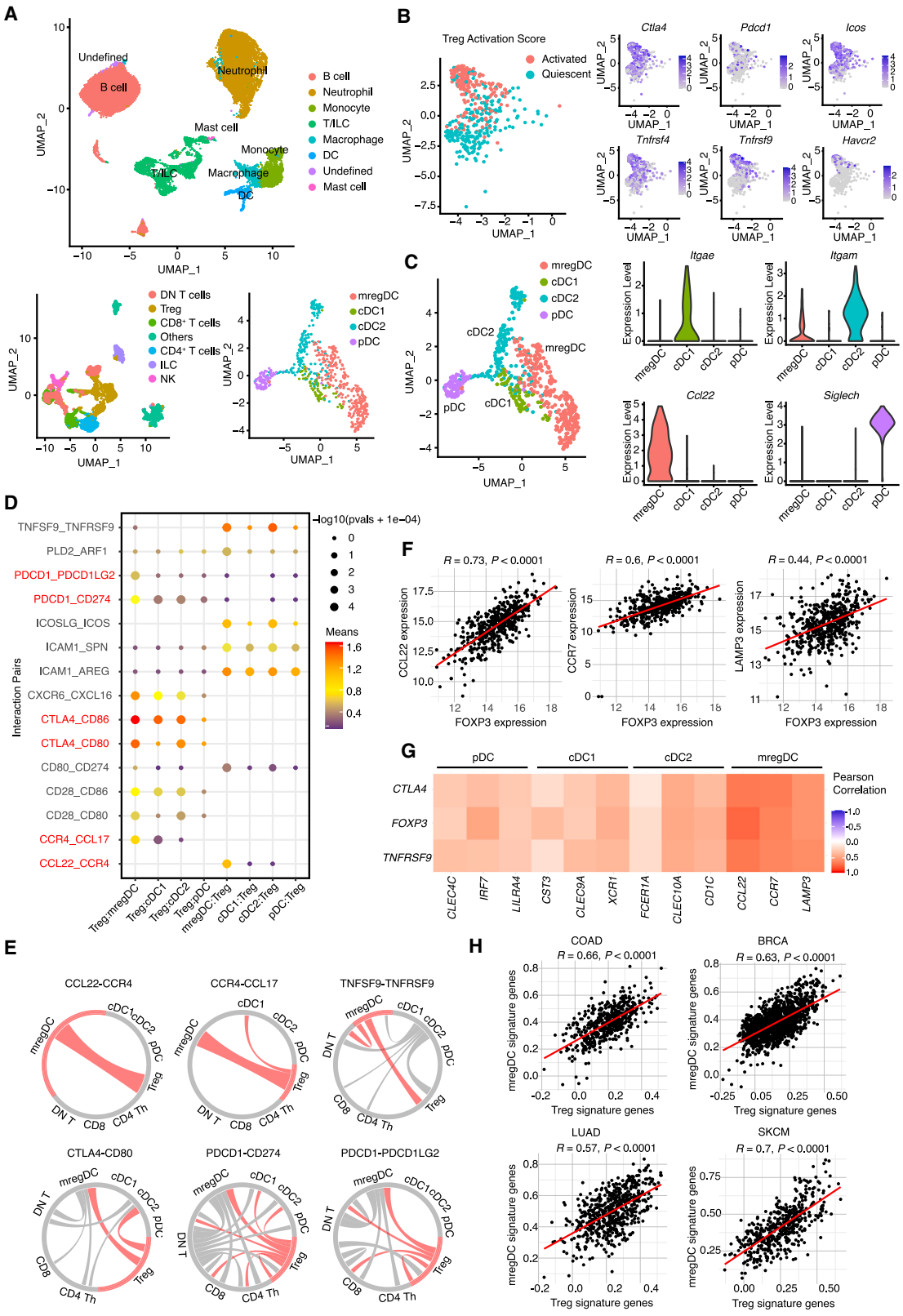

Figure 2. Transcriptome analysis reveals a correlation between Treg and mregDC in mouse and human cancers

(A) Uniform manifold approximation and projection (UMAP) plots showing clusters of all immune cells isolated from colon tissues of wild-type mice and tumors of *Apc*$^{Min/+}$ mice by scRNAseq (upper panel). Lower panels showing T/ILC (lower left) and DC (lower right) clusters.

(legend continued on next page)

Tregs not only aligned with our flow cytometry data (Figure S3D), but also agreed with human tumor Treg phenotype in non-small-cell lung cancer and colorectal cancer.[20,21]

Generally, Treg activation involves TCR signaling in response to antigen recognition on DCs.[16,18] We therefore sought to identify DC subpopulations in the tumor that could induce Treg activation. Based on the scRNA-seq data, four DC sub-clusters were identified: *Siglech*$^+$ plasmacytoid DCs (pDCs), *Itgae*$^+$ cDC1s, *Itgam*$^+$ cDC2s, and *Ccl22*$^+$ DCs (Figures 2C and S4G). Compared to other subpopulations, CCL22$^+$ DCs expressed higher levels of maturation-related, migration, and regulatory genes, while exhibiting lower levels of Toll-like receptor signaling-associated genes (Figure S4H). These gene expression signatures were similar to those characteristic of DC3,[5,42] mregDC,[39] and *LAMP3*$^+$ DC[38] found in various mouse and human tumors. Therefore, we use "mregDC" to describe this cell cluster in the following study. To explore the potential association between activated Tregs and these distinct DC subpopulations, we conducted a set of immune-related ligand-receptor (L-R) pair analyses using the CellPhoneDB algorithm.[55] In total, 105 L-R pairs were predicted to mediate interactions between Tregs and various DC clusters, among which 76, 41, 84, and 63 were associated with mregDCs, cDC1s, cDC2s, and pDCs, respectively (Table S1). Although cDC2s were predicted to have the most L-R pairs, mregDCs exhibited more specific chemotactic axes (CCL17/CCL22-CCR4 and CXCL16-CXCR6) and stronger surface molecule interaction potential with Tregs (CD274/PDCD1LG2-PD-1, CD80/CD86-CTLA-4/CD28, TNFSF9-TNFRSF9, and ICOSL-ICOS), owing to higher expression of those genes (Figures 2D, 2E, and S4I). These predictions suggest that mregDCs are the most likely candidates to attract and physically interact with Tregs in the TME.

To look for an association between mregDCs and Tregs in human cancers, we analyzed RNA-seq datasets from colon adenocarcinoma patients available through The Cancer Genome Atlas (TCGA) Project. Our findings revealed a significant correlation between the expression of *FOXP3* and human mregDC signature genes (*CCL22*, *CCR7*, and *LAMP3*) (Figure 2F). Additionally, we evaluated the relationship between Treg and various DC clusters with multiple signature genes (*CTLA4*, *FOXP3*, and *TNFRSF9* for Tregs; *CLEC4C*, *IRF7*, and *LILRA4* for pDCs; *CST3*, *CLEC9A*, and *XCR1* for cDC1s; *FCER1A*, *CLEC10A*, and *CD1C* for cDC2s; *CCL22*, *CCR7*, and *LAMP3* for mregDCs). Similar to the mouse data, gene expression characteristic of human Tregs was preferentially correlated with mregDCs compared to other DC subpopulations (Figure 2G). Given the prevalence of mregDCs in various human TME,[41] they were highly correlated with Tregs in multiple cancer types from the TCGA database, such as breast invasive carcinoma (BRCA), lung adenocarcinoma (LAUD), and skin cutaneous melanoma (SKCM) (Figure 2H). These data indicate that the correlation between Tregs and mregDCs is a common feature in both human and mouse tumors.

The Treg-mregDC-lymphatic niche is established in the tumor stroma

Surface ligand-receptor interactions between Tregs and mregDCs imply a close proximity within the TME. Therefore, we investigated their spatial relationships and associations with lymphatic vessels in *Apc*$^{Min/+}$ tumors. Notably, within the tumor stroma, CD11c$^+$ DCs co-localized with Tregs surrounding the lymphatic vessels (Figure 3A). Given the transcriptomic evidence suggesting an intimate relationship between Tregs and mregDCs, we crossed *Ccl22*^{tdTomato} reporter mice[56] with *Apc*$^{Min/+}$ mice to specifically identify mregDCs. Although previous studies indicated that CCL22 was produced by tumor-associated macrophages,[57,58] single-cell transcriptomic analysis conclusively identified DCs, particularly mregDCs, as the only cell population transcribing the *Ccl22* and *Ccl17* genes in *Apc*$^{Min/+}$ tumors (Figures S5A and S5B). This expression of CCL22 by DCs was further confirmed by flow cytometry (Figures S5C and S5D). Moreover, immunofluorescence images revealed that tdTomato expression was exclusively observed in CD11c$^+$ cells displaying dendritic morphology, affirming the reliability of this reporter in detecting the mregDC state (Figure 3B). These tdTomato-marked mregDCs were closely associated with Tregs in the peri-lymphatic region, forming what we now recognize as a Treg-mregDC-lymphatic niche (Figure 3B and Video S2). A recent study demonstrated that CXCR3 expression on Tregs drives their co-localization with CXCL9-producing cDC1s in tumor.[30] Therefore, we visualized the distribution of cDC1s and cDC2s alongside mregDCs in the tumor stroma and examined their associations with lymphatics and Tregs. Compared to cDC1s and cDC2s, mregDCs were more preferentially positioned in the peri-lymphatic region (Figures 3C–3E) and in closer proximity to Tregs (Figure 3F). Consistent with previous observations that CCR7$^+$ mregDCs clustered in perivascular niche,[42] we found that, in contrast to blood vessels, mregDCs were notably enriched in the peri-lymphatic region (Figure S5E). This enrichment correlated with the expression of the CCR7 ligand CCL21, primarily produced by lymphatic endothelial cells rather than blood vessels (Figure 3G). Considering that mregDCs appear to represent an activated/mature state, characterized by high expression of maturation- and migration-associated genes (Figure S4H), their peri-lymphatic location aligns with the notion that these cells are predisposed to migrate to tdLNs through lymphatic vessels.

Considering the consistent co-occurrence of mregDCs and Tregs in many human tumor types (Figure 2H), including but

(B) UMAP plots showing activation scores (left) and individual gene expression (right) in tumor Tregs.
(C) UMAP plots of tumor DC clusters (left) and violin plots of their feature genes (right).
(D) CellPhoneDB ligand-receptor pair analysis between Treg and DC clusters.
(E) Chord diagram showing preferential interactions between T cell and DC clusters.
(F) Correlation between mregDC signature genes and *FOXP3* in TCGA datasets for colorectal adenocarcinoma (COAD).
(G) Heatmap showing the Pearson-correlation of the signature genes for DC clusters and Tregs in TCGA COAD datasets.
(H) Correlation between mregDC and Treg signature genes in multiple tumors from TCGA datasets. Pearson-correlation coefficient R and two-sided *p* value are shown in (F and H).
See also Figures S3 and S4 and Table S1.

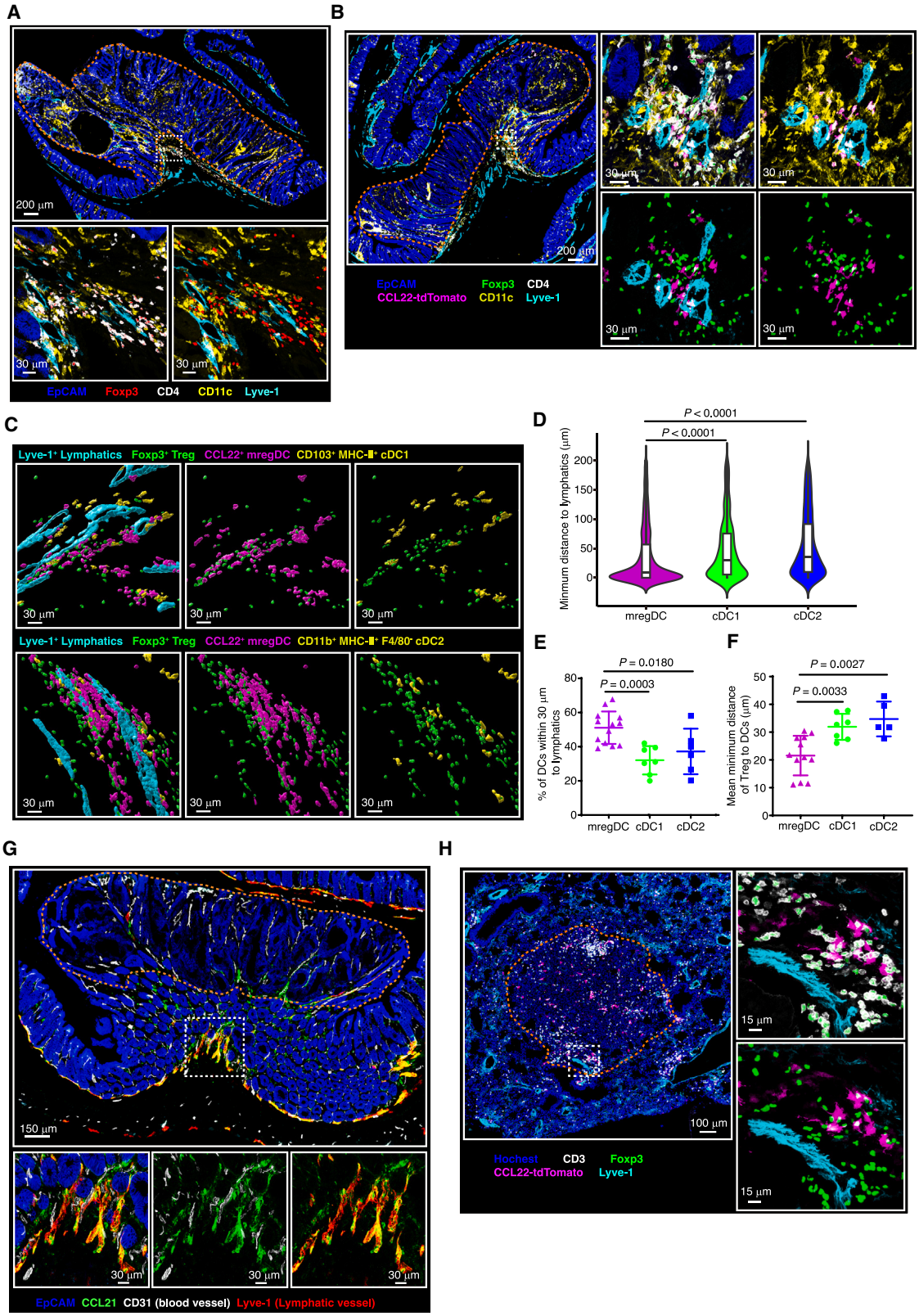

Figure 3. The Treg-mregDC-lymphatic niche is established in colorectal and lung cancers

(A) Immunofluorescence staining of Tregs, DCs, and lymphatic vessels in colon tumors from *Apc*$^{Min/+}$ mice.

(B) Immunofluorescence staining showing the association of mregDCs with Tregs in the peri-lymphatic region of colon tumors from *Apc*$^{Min/+}$ *Ccl22*^{tdTomato} mice.

(legend continued on next page)

not limited to colon adenocarcinoma, lung adenocarcinoma, breast invasive carcinoma, and skin cutaneous melanoma, we questioned whether this Treg-mregDC-lymphatic niche might also be present in the TME of other mouse models. To our delight, an identical niche was discernible in lung adenocarcinomas generated by intravenous injection of the KP (*Kras*^{G12D}/*p53*$^{-/-}$) tumor cell line into *Ccl22*^{tdTomato} reporter mice (Figure 3H). These compelling findings strongly suggest that the existence of this niche is not confined to colorectal cancer alone but extends to other tumor types, underscoring its broader relevance in tumor immunology.

Tregs are activated by mregDC in peri-lymphatic niche

Both scRNAseq and flow cytometry data unveiled the heterogeneous states of Tregs within TME (Figures 2B and S3D), with some being activated while others remained quiescent. This phenotypic heterogeneity could be a result of their distinct microenvironments.[59] To investigate the intricate relationship between fine-grained spatial organization and Treg activation, we employed the T cell activation markers PD-1 and OX-40 along with Foxp3 to delineate "activated" Tregs. Histo-cytometry analysis revealed that the majority of PD-1^{high} and OX-40 ^{high} Treg were positioned in close proximity to mregDCs (Figures 4A–4D). Although PD-1^{high} or OX-40 ^{high} Tregs were adjacent to mregDCs, it remains plausible that their activation occurred elsewhere, such as in lymph nodes, before being recruited to mregDCs in TME. To ascertain whether Tregs were locally activated in the TME, we crossed *Apc*$^{Min/+}$ *Ccl22*^{tdTomato} mice with Nur77 reporter (*Nr4a1*^{GFP}) mice,[60] an immediate-early response gene, enabling us to visualize TCR signaling *in situ*. Indeed, we observed a fraction of Tregs in tumor stroma expressing GFP (Figure 4E). These GFP^{+} Tregs were situated significantly closer to mregDCs than to cDC1s and cDC2s (Figure 4F), suggesting that Tregs likely acquired their activation state through local crosstalk with mregDCs. Given that peptide-MHC-II-TCR signaling is a primary driver of T cell activation, we administered a blocking antibody targeting I-A^{b}, the MHC class II molecule, into tumors of *Apc*$^{Min/+}$ animals. Following treatment, we observed a significant reduction in the proliferation and total number of Tregs, accompanied by decreased expression levels of activation-related molecules, including PD-1, CTLA-4, TIM-3, OX-40, and ICOS (Figures 4G–4J). This impaired Treg activation upon anti-MHC-II treatment was further confirmed by the immunofluorescence (Figures 4K and 4L). However, MHC-II blockade did not impact the association of Tregs with mregDCs in the peri-lymphatic region (Figures 4K and 4L), indicating that MHC-II-TCR signaling is essential for Treg activation but not for the formation of Treg-mregDC-lymphatic niche in the TME. Interestingly, we also noted that blocking the crosstalk between Tregs and mregDCs resulted in a closer distribution of mregDCs to lymphatic vessels (Figures 4K and 4L). Collectively, these findings suggest that the crosstalk between Tregs and mregDCs fosters a highly activated state in Tregs and thus enhances their suppressive functions within the TME.

CCR4 is critical for Treg recruitment to mregDC in peri-lymphatic region and tumor progression

In addition to the direct contact between Tregs and mregDCs through surface molecular interactions, these two cell types were also intricately associated via chemokines and chemokine receptors, notably CCL22/17-CCR4 and CXCL16-CXCR6 (Figure 2D). It is well established that Tregs constitutively express CCR4, which drives their infiltration into tumor site in multiple cancer types.[57,61,62] Considering our preceding data indicated that mregDCs were most likely recruited to lymphatic vessels via CCL21-CCR7 chemotaxis, if CCR4^{+} Tregs are in turn attracted to mregDCs, this would explain the formation of the niche. We therefore crossed *Ccr4*$^{-/-}$ mice with *Apc*$^{Min/+}$ mice. However, very few tumor foci were observed in both small intestine and colon in *Apc*$^{Min/+}$ *Ccr4*$^{-/-}$ mice (Figures S6A and S6B). To eliminate the possibility that the absence of CCR4 on cell types other than Tregs might be responsible for inhibiting tumor growth, we generated mice with Treg-specific CCR4 deficiency on the *Apc*$^{Min/+}$ background (*Apc*$^{Min/+}$ *Foxp3*^{Cre} *Ccr4*$^{fl/fl}$). Like the germline *Ccr4* knockout mice, specific deletion of CCR4 on Tregs effectively halted tumor growth (Figures 5A and 5B). This outcome indicates a non-redundant role of CCR4 in driving Treg infiltration into tumor site, where they establish a suppressive TME and promote tumor immune evasion. While these approaches precluded direct examination of the niche in such animals, the results were consistent with the significance of the Treg-mregDC interaction and this association in suppressing anti-tumor immunity. In the absence of this suppressive axis, the immune system gains the ability to inhibit tumor growth more effectively.

Although this interpretation of CCR4-CCL22 interaction and its impact on Treg function was consistent with the data, other explanations for the failure of tumor growth in these conditions could be imagined. To delve further into this issue, Tregs were isolated from *Ubi-tdTomato* mice and mixed with *Ubi-GFP* (WT + WT) or *Ccr4*$^{-/-}$ *Ubi-GFP* (WT + *Ccr4*$^{-/-}$) Tregs, and transferred into 4-month-old *Apc*$^{Min/+}$ mice that had already developed tumors (Figure 5C). One week later, we quantified the different fluorescent protein-labeled Tregs in the mesenteric lymph nodes (mLNs) and tumors. As expected, both wild-type and *Ccr4*-deficient GFP^{+} Tregs were equally abundant in the mLNs as their tdTomato^{+} counterparts. However, a reduced number of *Ccr4*$^{-/-}$ Tregs were recruited into the tumors

(C) Surface reconstruction of images showing the association of mregDCs (MHC-II^{+} tdTomato^{+}), cDC1s (MHC-II^{+} tdTomato^{-} CD103^{+}), and cDC2s (MHC-II^{+} tdTomato^{-} CD11b^{+} F4/80^{-}) with Tregs in the peri-lymphatic region of colon tumors from *Apc*$^{Min/+}$ *Ccl22*^{tdTomato} mice.
(D–F) Quantification of the minimal distance of each DC to lymphatic vessels (D), DCs within 30 μm of lymphatic vessels (E), and the mean minimum distance between Tregs and DC clusters (F) based on (C). For the violin-box plots in (D), the centerlines indicate the median. The box limits indicate the first and third quartiles. The whiskers indicate the maxima and minima. Graphs in (E–F) show mean ± SD. Statistical significance was calculated by unpaired two-tailed Student's t test (D-F). Each dot represents data from an individual tumor, results are pooled from two independent experiments.
(G) Immunofluorescence staining of CCL21 in colon tumors from *Apc*$^{Min/+}$ mice.
(H) Immunofluorescence staining of the Treg-mregDC-lymphatic niche in lung adenocarcinoma. The dashed orange and white lines mark the tumor and magnified ROI, respectively. Images are representative of at least five tumor sections from five mice.
See also Figure S5 and Video S2.

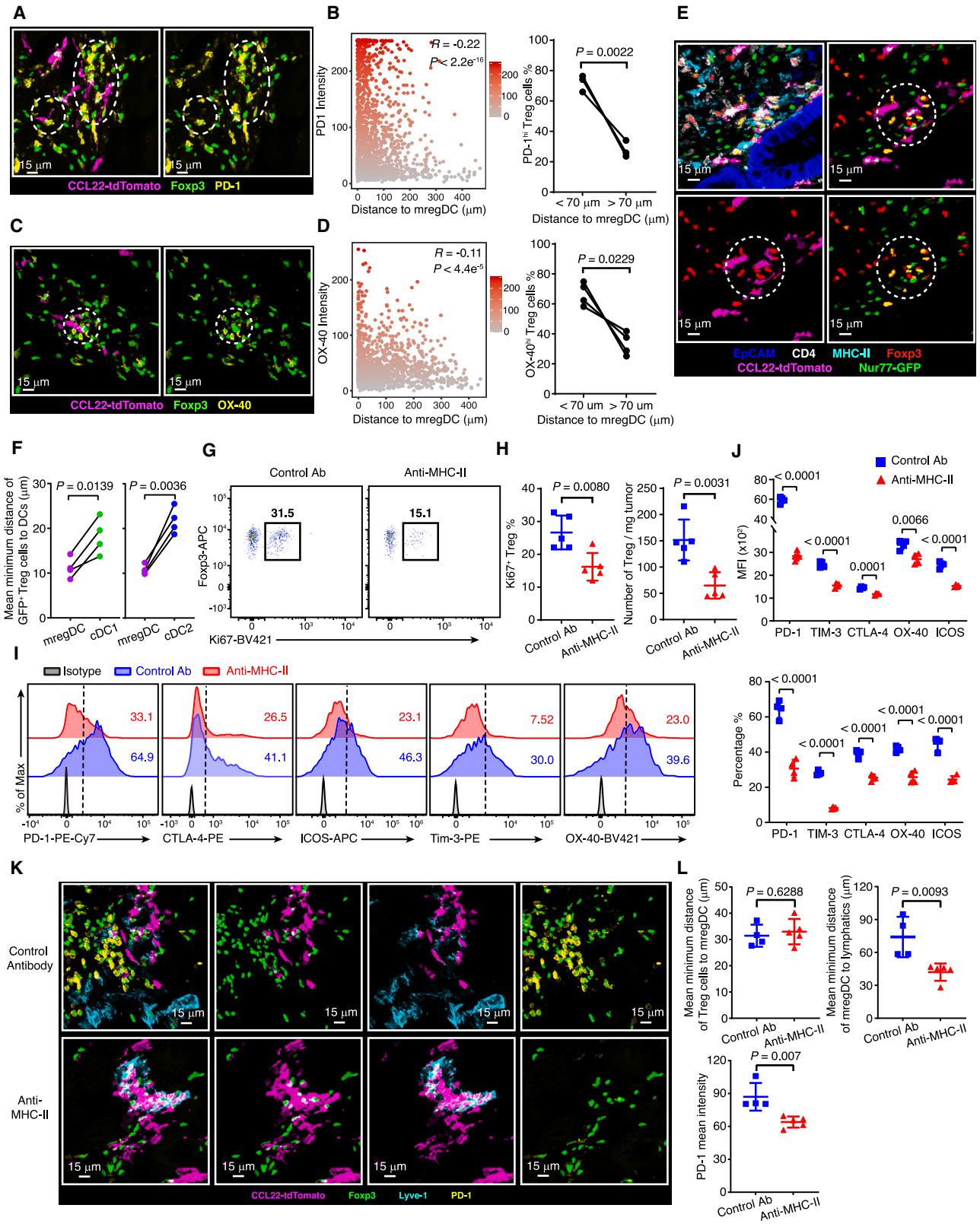

(legend on next page)

(Figures 5D and 5E). More strikingly, in contrast to WT Tregs, where a substantial proportion exhibited an activated state, very few *Ccr4*$^{-/-}$ Tregs in tumors expressed activation-associated molecules (Figures 5F and S6C). It's worth noting that in this transfer experiment, endogenous Tregs had already infiltrated into the stromal niche at the time of introducing labeled cells, which may have interfered with the subsequent recruitment of new Tregs into the tumors. To overcome this circumstance, we generated mixed bone marrow chimeras using a similar strategy to examine the accumulation of Tregs within the tumor under physiological conditions (Figure S6D). Again, the absence of CCR4 hampered Treg recruitment to the tumor (Figures S6E and S6F). To further investigate whether CCL22/17-CCR4 axis is essential for the formation of the Treg-mregDC-lymphatic niche and subsequent Treg activation, we generated mixed bone marrow chimeras by transplanting *Ccl22*^{tdTomato} and *Ccr4*$^{-/-}$ *Ubi-GFP* bone marrow cells into irradiated *Apc*$^{Min/+}$ mice (Figure 5G). In the absence of CCR4, very few GFP^{+} Tregs were recruited to mregDCs compared to their GFP^{-} counterparts (Figures 5H and 5I). Importantly, within the Treg-mregDC-lymphatic niche, the majority of PD-1^{+} Tregs originated from GFP^{-} *Ccl22*^{tdTomato} rather than GFP^{+} *Ccr4*$^{-/-}$ bone marrow cells (Figures 5H and 5I), indicating that proper positioning of Tregs is a prerequisite for their functional states. Since CCL22 was exclusively expressed by mregDCs, these results together suggest that Tregs were particularly recruited to mregDC niche in tumor stroma by chemotaxis, where they acquired activation states, thereby establishing a suppressive micro-environment and facilitating tumor immune evasion.

Tregs restrain tumor antigen transportation to draining lymph nodes and limit the initiation of anti-tumor immune responses

Next, we asked how Tregs exert their suppressive influence on anti-tumor immunity within the Treg-mregDC-lymphatic niche. The initiation of a successful antigen-specific adaptive anti-tumor immune response relies on DCs, which take up tumor antigens within the tumor lesion and simultaneously acquire a mature state. Subsequently, these mature DCs upregulate CCR7 and migrate through the lymphatic vasculature to the tdLNs, where they present the antigens to T cells. Once primed by tumor antigen-bearing migratory DCs, tumor-reactive T cells undergo proliferation, differentiation and infiltration into the tumors to carry out their effector functions.[32,63–66] MregDCs possess all the characteristics of mature DCs capable of initiating anti-tumor immune responses. However, their close interactions with Tregs in the peri-lymphatic region led us to speculate that Tregs might be impeding DC migration to the draining lymph nodes. To investigate this hypothesis, we measured migratory DCs (mDCs) and lymph node-resident DCs (rDCs) in the tumor-draining mLNs, distinguished by the expression levels of CD11c and MHC-II (mDCs, CD11c^{int} MHC-II^{high}; rDCs, CD11c^{high} MHC-II^{int}) (Figure S7A).[67,68] Intriguingly, a majority of CD11^{int} MHC-II^{high} mDCs, but very few CD11^{high} MHC-II^{low} rDCs, expressed CCL22 (Figure S7B), confirming the migratory property of the mregDCs. Interestingly, compared to wild-type mice, mDCs were significantly reduced in the mLNs of tumor-bearing *Apc*$^{Min/+}$ mice (Figures 6A–6C). The same phenomenon was observed in *Villin*^{Cre} *Apc*$^{fl/+}$ mice (Figures S7C–S7E), suggesting that the migration impairment of DCs was due to tumor-related effects rather than an intrinsic defect resulting from gene mutation.

Compared to the entire migratory DC population, which represented the overall migration of DCs from the entire intestine, including tumor and normal tissue, we were particularly interested in migratory DCs carrying tumor antigens. To discern these antigen-presenting cells, we conducted an experiment wherein fluorescent dye-conjugated ovalbumin (FITC-OVA) was co-administered with lipopolysaccharide (LPS) *in situ* into the colon or tumor to simulate tumor antigens. Twenty-four hours later, FITC^{+} DC populations were examined in the mLNs. As anticipated, migratory DCs were the dominant population responsible for transporting antigens from peripheral tissue to the lymph nodes. However, this capacity was markedly impaired in the tumor-bearing mice (Figures 6D, 6E, S7F, and S7G). Furthermore, when FITC-OVA/LPS-treated mice were transferred with fluorescent dye-labeled OT-I or OT-II T cells, which specifically recognize OVA peptides presented by MHC-I or MHC-II molecules, respectively, and these transferred cells were trapped in lymphoid tissues using the sphingosine 1-phosphate (S1P) antagonist FTY720 (Figure 6F), both OT-I and OT-II cell proliferation was reduced in tumor-bearing *Apc*$^{Min/+}$ mice (Figures 6G–6I and S7H–S7J), consistent with the reduced antigen presentation.

To test whether Tregs were responsible for impaired tumor antigen presentation, we depleted Tregs in *Apc*$^{Min/+}$ *Foxp3*^{DTR} mice and then performed intra-tumor injection of FITC-OVA/LPS (Figure 6J). Following Treg depletion, there was a remarkable increase in tumor antigen-bearing mDCs in the mLNs (Figures 6K and 6L). Given that Tregs were tightly associated with mregDCs

Figure 4. Tregs are locally activated on mregDCs

(A and C) Immunofluorescence staining of PD-1 (A) and OX-40 (C) on Tregs and their association with mregDCs in colon tumors of *Apc*$^{Min/+}$ *Ccl22*^{tdTomato} mice.
(B and D) Correlation between the intensity of PD-1 (B) and OX-40 (D) on Tregs and their distance to mregDCs (left), and quantification of PD-1^{high} and OX-40^{high} Tregs associated with mregDCs (right).
(E) Immunofluorescence staining of Nur77-GFP^{+} Tregs within Treg-mregDC niche in tumors of *Apc*$^{Min/+}$ *Ccl22*^{tdTomato} *Nr4a1*^{GFP} mice.
(F) Quantification of the mean minimum distance of Nur77-GFP^{+} Tregs to various DCs.
(G and H) Representative flow cytometry plots (G) and quantification (H) of Ki67^{+} Tregs and total number in colon tumors from *Apc*$^{Min/+}$ mice following intra-tumor injection of control or anti-I-A^{b} antibody.
(I and J) Representative histograms (I) and quantified expression of (J) T cell activation-related molecules on tumor Tregs from *Apc*$^{Min/+}$ mice treated as (G). Upper panel, mean fluorescence intensity (MFI); lower panel, percentage.
(K) Immunofluorescence staining of PD-1 expression on Tregs within Treg-mregDC-lymphatic niche in tumors of *Apc*$^{Min/+}$ *Ccl22*^{tdTomato} mice treated as (G).
(L) Quantification of the mean minimum distance of Tregs to mregDCs (upper left), the mean minimum distance of mregDCs to lymphatics (upper right), and the mean intensity of PD-1 expression on Tregs (lower panel) based on (K). Images are representative of at least four tumor sections from four mice (A, C, E, and K). Graphs in (H, J, and L) show mean ± SD. Each dot represents data from an individual mouse; results are pooled from two independent experiments (B, D, F, H, J, and L). Statistical significance was calculated by unpaired (H, J, and L) and paired (B, D, and F) two-tailed Student's t test.

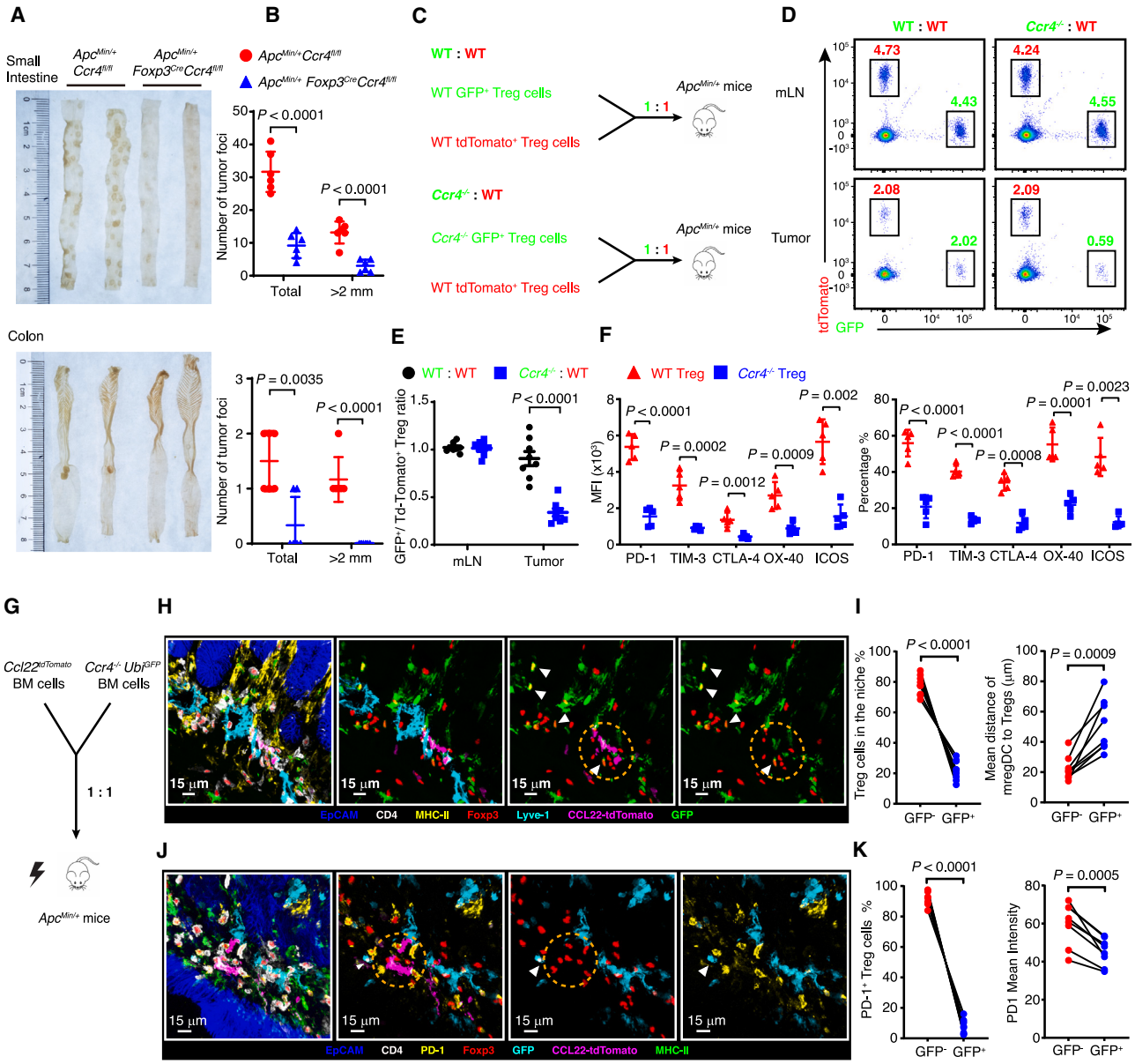

Figure 5. *Ccr4* is critical for Treg-mregDC-lymphatic niche formation and tumor growth

(A and B) The representative image (A) and quantification of tumor foci (B) in small intestine (upper panel) and colon (lower panel) from 14-week-old $Apc^{Min/+}Ccr4^{fl/fl}$ and $Apc^{Min/+}Foxp3^{cre}Ccr4^{fl/fl}$ mice.

(C) Experimental design for (D–F).

(D–F) Representative flow cytometry plots (D), quantified ratio of Treg in mesenteric lymph nodes (mLN) and tumor (E) and expression of T cell activation-related molecules (F) on different subsets of Tregs within tumors from $Apc^{Min/+}$mice transferred with tdTomato$^+$ WT and GFP$^+$ $Ccr4^{-/-}$ or GFP$^+$ WT Tregs mixed at 1:1 ratio on day 5 post transfer.

(G) Experimental design for (H–K). Tumors were harvested 12 weeks after bone marrow reconstitution.

(H and J) Representative immunofluorescence imaging showing the association of mregDC with CCR4-competent or -deficient Tregs (H) and PD-1 expression on Tregs (J) in colon tumors. Images are representative of seven tumor sections from seven mice.

(I) Quantification of the Treg subsets within the Treg-mregDC-lymphatic niche (left panel) and the mean minimum distance between Tregs and mregDCs.

(K) Quantification of PD-1^{high} Tregs (left panel) and mean intensity of PD-1 expression (right panel) within the Treg-mregDC-lymphatic niche. The white arrow heads mark the GFP$^+$ $Ccr4^{-/-}$ Tregs. Graphs in (B, E and F) show mean ± SD. Each dot represents data from an individual mouse; results are pooled of two independent experiments (B, E, F, I, and K). Statistical significance was calculated by unpaired (B, E, and F) and paired (I and K) two-tailed Student's t test. See also Figure S6.

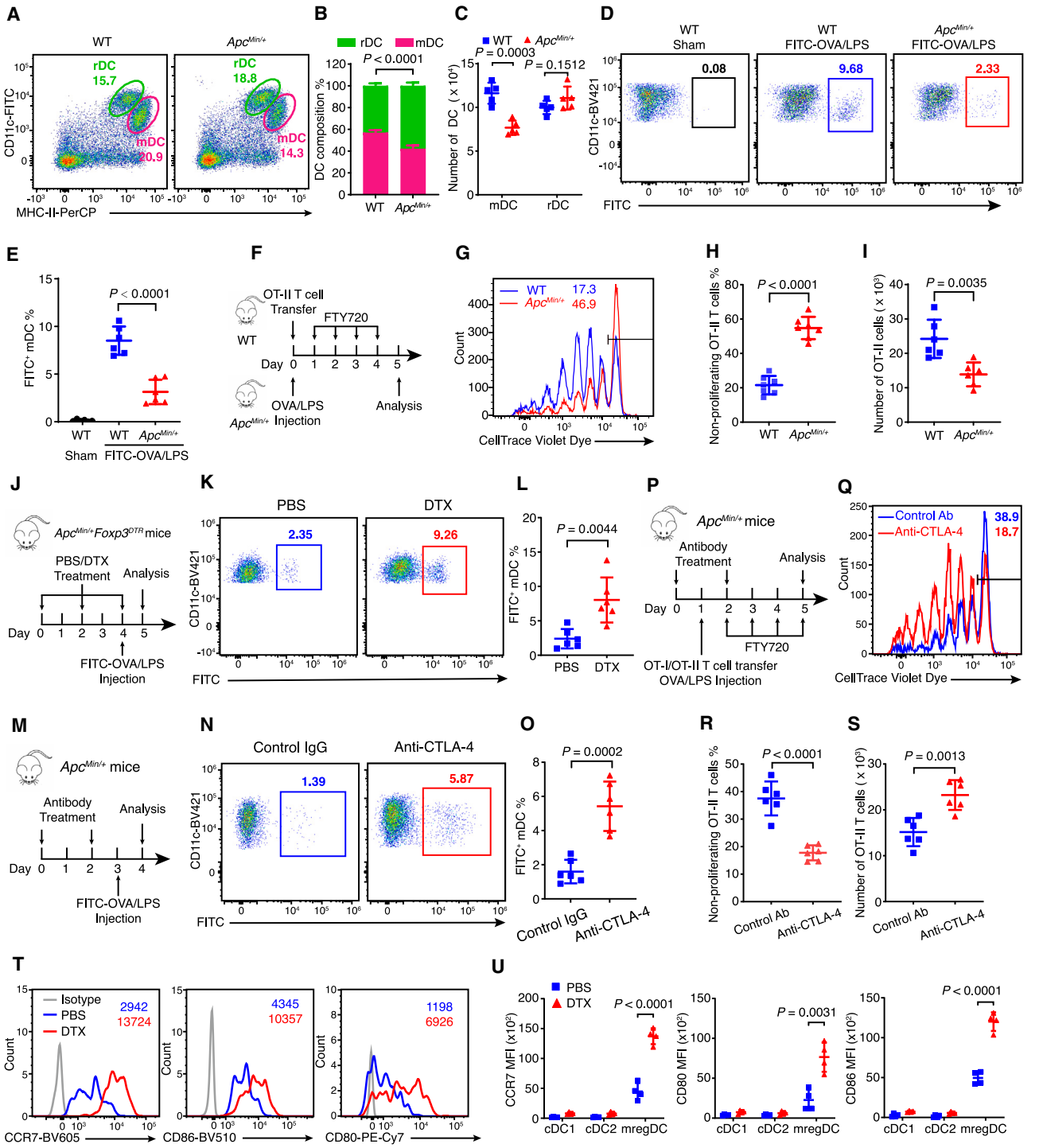

Figure 6. Tregs restrain tumor antigen transportation to tumor-draining lymph nodes and limit initiation of anti-tumor immune responses

(A–C) Representative flow cytometry plots (A), quantification of the proportion (B), and absolute number (C) of mDCs and rDCs in mLNs from 14-week-old WT and *Apc*$^{Min/+}$ mice.

(D and E) Representative flow cytometry plots (D) and quantification (E) of FITC$^+$ mDCs in mLNs 24 h after intra-colon or intra-tumor injection of FITC-OVA/LPS into WT or *Apc*$^{Min/+}$ mice, respectively.

(F) Experimental design for (G–I).

(G–I) Representative histograms (G), quantified non-proliferating (H) and absolute number (I) of CellTrace Violet-labeled OT-II cells in mLNs from WT or *Apc*$^{Min/+}$ mice treated as in (F).

(J) Experimental design for (K and L).

(legend continued on next page)

in peri-lymphatic niche and CTLA-4 was a dominant molecule for Treg suppressive functions, we sought to disrupt Treg-mregDC interaction using an anti-MHC-II blockade or a non-depleting anti-CTLA-4 antibody (Figure 6M). Both antibody treatments significantly improved tumor antigen trafficking to the tdLNs (Figures 6N, 6O, S7K, and S7L). To assess whether enhanced tumor antigen trafficking could facilitate T cell priming, we transferred OT-I and OT-II T cells into mice treated with anti-CTLA-4 or control antibody (Figure 6P). As anticipated, the proliferation of both OT-I and OT-II cells substantially increased following anti-CTLA-4 treatment (Figures 6Q–6S and S7M–S7O). Lastly, to elucidate the mechanisms underlying the enhanced tumor antigen transportation following Treg depletion or anti-CTLA-4 treatment, we analyzed phenotypical changes in mregDCs, cDC1s and cDC2s in the TME. While mregDCs exhibited higher expression levels of CCR7, CD80, and CD86 compared to cDC1s and cDC2s before treatment, these molecules were specifically upregulated in mregDCs following Treg depletion or anti-CTLA-4 treatment, with minimal changes observed in cDC1s and cDC2s (Figures 6T, 6U, and S7P–S7R). These results indicate that mregDCs are the primary targets of Tregs for their suppressive functions. Taken together, our findings suggest that the crosstalk between Tregs and mregDCs in the TME restrains the initiation of anti-tumor immune responses by inhibiting the transportation of tumor antigens to the draining lymph nodes.

The establishment of Treg-mregDC-lymphatic niche in human cancer predicts worse outcome

While transcriptomic analysis has indicated a high degree of correlation between Tregs and mregDCs in human cancers (Figures 2F–2H), their spatial relationship in clinical cohorts required further investigation. Therefore, we analyzed recently published spatial transcriptomic data on human colorectal cancer (CRC).[69] Employing a comprehensive approach based on cell state signature genes (Table S2) for cell localization analysis, we discovered a notable clustering of activated Tregs with mregDCs in the peri-lymphatic region of the tumor stroma (Figures 7A and S8A), resembled the Treg-mregDC-lymphatic niche observed in the mouse $Apc^{Min/+}$ tumor. Additionally, quantitative spatial statistical analysis highlighted that activated Tregs exhibited closer proximity to mregDCs than quiescent Tregs (Figures 7B and S8B). These distinctive spatial characteristics were consistently observed across all 14 sections from the 7 patients included in this study (Figures 7C and S8C), suggesting that the crosstalk between Tregs and mregDCs in the peri-lymphatic region represents a ubiquitous organization of the suppressive TME in human colorectal cancer.

Next, we investigated whether this spatial crosstalk between Tregs and mregDCs was relevant to the survival outcomes of COAD cohorts from the TCGA dataset. To gain a deeper understanding of the combined impact of activated Tregs and mregDCs on patient prognosis, we categorized patients into two groups based on their mregDC signature score, calculated by the ssGSEA algorithm. We then explored the influence of activated Treg signature genes ($actTreg^{high}$ or $actTreg^{low}$) on patient outcomes within the $mregDC^{high}$ group. Notably, the $mregDC^{high}$ $actTreg^{low}$ group exhibited a significantly improved prognosis in terms of overall survival, progression-free survival, and disease-free survival in comparison to the $mregDC^{high}$ $actTreg^{high}$ group, while the survival rate of $mregDC^{high}$ $actTreg^{high}$ patients was comparable to that of the $mregDC^{low}$ group (Figure 7D). This pattern of association remained consistent across both microsatellite stable (MSS) and microsatellite instability (MSI) patient cohorts (Figures 7E and S8D). These findings underscore the dominant role of the interplay between mregDCs and Tregs in regulating human tumor progression, regardless of tumor mutation loads or lymphocyte infiltration. Although previous study demonstrated that expression levels of mregDC signature genes (*CCL22* and *CCR7*) correlated with anti-tumor immune response and favorable survival outcomes in colorectal cancer patients,[40] our current findings indicate that the presence of activated Tregs establishes a suppressive microenvironment that impedes mregDC-mediated anti-tumor immune responses.

Finally, to evaluate the broader implications of the interaction between activated Tregs and mregDCs in human cancers, we extended our analysis to encompass all TCGA tumor types. Within this comprehensive examination, we identified a total of ten TCGA cohorts, particularly kidney renal clear cell carcinoma (KIRC) and rectum adenocarcinoma (READ), where individuals with lower expression levels of activated Treg gene signature showed substantial survival advantages compared to those bearing the $actTreg^{high}$ $mregDC^{high}$ signatures (Figures 7F and S8E). These findings collectively underscore that, similar to observations in murine models, the lymphatic-localized crosstalk between Tregs and mregDCs constitutes an inhibitory microenvironment hindering anti-tumor immune responses, which is consistently associated with reduced survival across various human cancer types.

DISCUSSION

Employing a combination of quantitative multiplex imaging, scRNAseq and mouse genetics tools, here we have identified a Treg-mregDC-lymphatic niche within the tumor stroma that

(K and L) Representative flow cytometry plots (K) and quantification of $FITC^+$ mDCs (L) in mLNs from $Apc^{Min/+}$ $Foxp3^{DTR}$ mice administered PBS or DTX together with intra-tumor injection of FITC-OVA/LPS.
(M) Experimental design for (N and O).
(N and O) Representative flow cytometry plots (N) and quantification of $FITC^+$ mDCs (O) in mLNs from $Apc^{Min/+}$ mice administrated with control or anti-CTLA-4 antibody together with intra-tumor injection of FITC-OVA/LPS.
(P) Experimental design for (Q–S).
(Q–S) Representative histograms (Q), quantified non-proliferating (R) and absolute number (S) of CellTrace Violet-labeled OT-II cells in mLNs from $Apc^{Min/+}$ mice administered control or anti-CTLA-4 antibody along with FITC-OVA/LPS and FTY720.
(T and U) Representative histograms (T) and quantified MFI (U) of CCR7, CD80 and CD86 expression on cDC1s, cDC2s and mregDCs from tumors of 16-week-old $Apc^{Min/+}$ $Foxp3^{DTR}$ $Ccl22^{tdTomato}$ mice administered PBS or DTX. Graphs in (B, C, E, H, I, L, O, R, S, and U) show mean ± SD. Each dot represents data from an individual mouse; results are pooled from two independent experiments. Statistical significance was calculated by unpaired two-tailed Student's t test.
See also Figure S7.

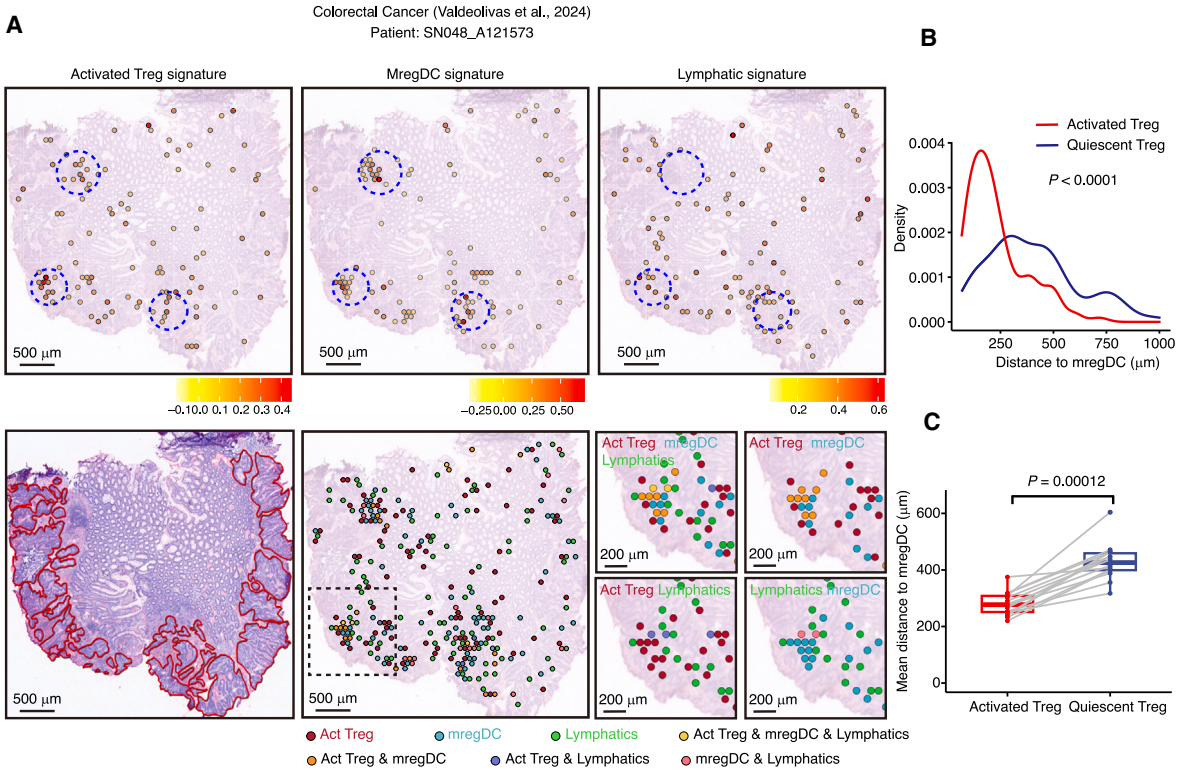

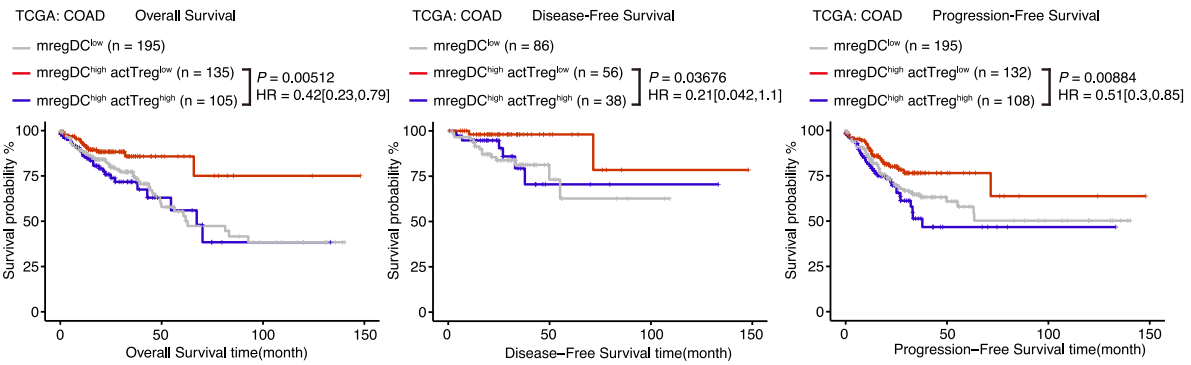

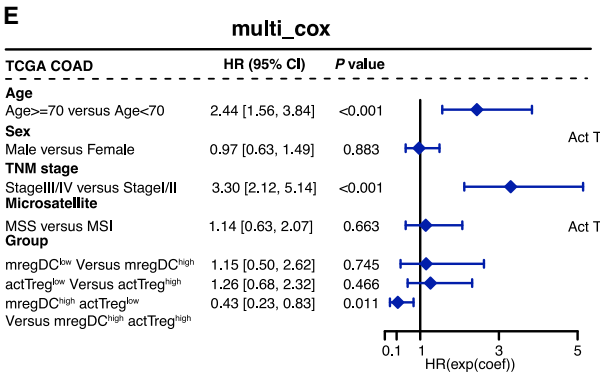

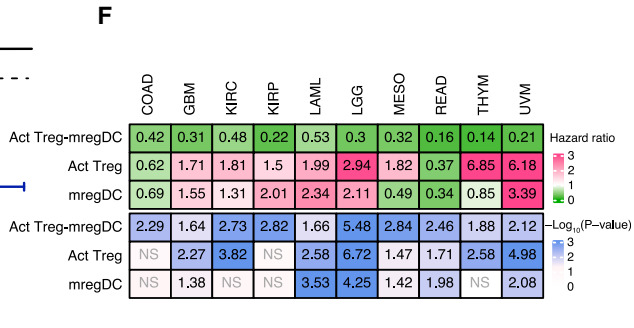

(legend on next page)

hinders tumor immune surveillance and promotes tumor progression. This suppressive niche is formed through a chemotactic axis involving CCL22/17-CCR4. The crosstalk between Tregs and mregDCs within this niche promotes Treg activation, characterized by high levels of surface co-stimulatory and inhibitory molecules, further enhancing the interaction with mregDCs. This reciprocal interaction hinders mregDC migration to tdLNs, limiting tumor antigen presentation and thereby impeding the initiation of anti-tumor immune responses. These findings provide an integrated view of how immunosuppressive TME is organized and emphasize how special immune architecture restrains anti-tumor immunity.

To unravel the intricacies of the TME, extensive endeavors have been taken using advanced approaches, such as scRNA-seq and mass cytometry (CyTOF), to elucidate the immune cell composition, heterogeneity, dynamic differentiation and potential functions in the context of tumor progression and immunotherapies.[3,70] These methods have provided invaluable insights into the cellular and molecular landscapes of various cancer types, as observed in both animal models and human samples. Nevertheless, due to lack of spatial information, the organization of various immune components in TME remains elusive. A pivotal contribution of this study lies in establishing a connection between the spatial network of immune cells and their responsive states, along with their associated functions. Tregs, recognized as the most important suppressive population, exhibit significant heterogeneity within the TME. This diversity includes both activated and quiescent states,[20,21,71] influenced by their specific locations. Our multiplex imaging approach delicately illustrates the spatial distinctions among different Treg states. Notably, within the peri-lymphatic region in tumor stroma, Tregs are strategically positioned in close proximity to mregDCs, which represent a mature state of DC marked with high expression of MHC-II and co-stimulatory molecules. These mregDCs consistently provide signals to Tregs, thereby sustaining their activated status. MHC-II blocking antibody effectively eliminates Treg activation signatures. Remarkably, this Treg-mregDC-lymphatic niche not only fosters the activated Treg phenotype, but also serves as the site where Tregs execute their suppressive functions. Upon activation, Tregs upregulate effector molecules, including CTLA-4, which inhibit the migration of mregDCs toward the tdLNs via lymphatic vessels. This action prevents the presentation of tumor antigens to T cells and the subsequent initiation of anti-tumor immunity. Therefore, our findings unveil a unique niche that reinforces the Treg activation state and serves as the backdrop for them to exert suppressive functions. Given the functional diversity of Tregs, our model is amenable to various spatial configurations and immune-modulating roles. In line with this, a recent study demonstrated that cDC1s recruit Tregs through the CXCL9-CXCR3 axis and promote their activation phenotype to locally suppress $CD8^+$ T cell activation in the tumor.[30] These collective findings suggest that Tregs may assume distinct functions depending on their specific neighboring cell types and spatial contexts.

Understanding the intricate immune architecture in the TME is pivotal for comprehending the complex nature of tumor immunology. A prior study has demonstrated that Tregs inhibit the migration of cDC2s toward tdLNs, thereby hindering the priming of effector $CD4^+$ T cells.[72] In our model, compared to cDC1s and cCD2s, mregDCs exhibit a mature signature and express higher levels of CCR7, indicating their propensity to migrate to tdLNs for tumor antigen presentation. Their close proximity to activated Tregs in the peri-lymphatic region suggests that mregDCs are *bona fide* targets of Treg-mediated suppression. Consistent with the observation that mregDCs originate from both cDC1 and cDC2 lineages,[38,39] we noted a significant impairment in the proliferation of both $CD4^+$ and $CD8^+$ T cells in tumor-bearing mice. This spatial organization of immune cells within the TME unveils novel mechanisms contributing to tumor immune evasion.

MregDC represent a unique molecular state that is adopted by both cDC1s and cDC2s upon uptake tumor antigens, endowing them with distinctive dual characteristics.[73,74] On one hand, they exhibit maturation signatures and express elevated levels of CCR7, facilitating their migration to the tdLNs, where they initiate the anti-tumor T cell responses.[39,65] Furthermore, mregDCs produce IL-12 and IL-15 to sustain T cell survival within the tumor and enhance their anti-tumor functions.[42] Conversely, mregDCs also possess high levels of immune checkpoint transcripts and other immunosuppressive genes, which could limit effector T cell functions. Our findings shed new light on the regulatory attributes of mregDCs. Notably, they secret CCL22 and CCL17, recruiting Tregs to the peri-lymphatic region to establish the suppressive Treg-mregDC-lymphatic niche. Subsequently, mregDCs promote the activation state of Tregs through MHC-II-TCR interactions and co-stimulatory signals. An intriguing discovery is that specific deletion of CCR4 on Tregs not only abolishes their correct distribution and activation state, also inhibits tumor progression. This underscores the pivotal regulatory roles of mregDCs

Figure 7. The establishment of Treg-mregDC-lymphatic niche in human cancers predicts worse survival rate

(A) Spatial mapping of activated Treg, mregDC and lymphatic signatures in tissue sections (upper) and their colocalization (lower right). Hematoxylin and eosin (H&E) staining of tissue sections matching the pathologists' tissue annotation (lower left). The red line, dashed blue circles and black square mark the tumor, the Treg-mregDC-lymphatic niches and magnified ROI, respectively.

(B) Spatial density of activated or quiescent Treg signature genes relative to their distance to mregDCs.

(C) Quantified mean distance of activated or quiescent Tregs to mregDCs in individual sections. In the box plots, the line represents the median, the box shows the interquartile range and the whiskers represent the range.

(D) Overall survival, disease-free survival and progression-free survival of TCGA COAD cohort based on the expression levels of mregDC and activated Treg signature genes.

(E) Multivariate Cox proportional-hazards model estimated the impact of different factors on the overall survival of COAD patients. Hazard ratios (HRs), 95% confidence intervals, and *p* values were shown in this table.

(F) Heatmap showing survival hazard ratio and *p* value of various cancer types, HR comparisons of indicated gene signatures. Statistical significance was calculated by paired (C) or unpaired two-tailed Wilcoxon test (B).

See also Figure S8 and Table S2.

in impeding anti-tumor immunity. Nevertheless, the mechanisms responsible for inducing these dual pro- and anti-tumor characteristics in mregDCs within the TME remain unknown. Deciphering the intricate regulatory effects of mregDCs has the potential to offer innovative strategies for future therapeutic applications.

By analysis of spatial transcriptomic data from human colorectal cancer, we uncovered a remarkable co-localization of mregDC signatures with activated Treg signatures, in concordance with our murine data. Furthermore, the identification of an identical niche in mouse lung cancer underscores the presence of this ubiquitous immune architecture. This compelling evidence strongly supports the existence of a general mechanism of Treg-mediated suppression across different cancer types in both mice and humans. Moreover, acquiring a deeper understanding of the spatial organization and interplays of immune cell populations enables more precise tumor prognosis predictions.[75] While mregDC signature is commonly associated with favorable tumor prognosis,[40,42] their crosstalk with Tregs attenuates the beneficial outcomes in multiple tumor types. Thus, depicting the spatial architecture will provide invaluable information for tumor prognosis prediction and guiding clinical therapeutic applications.

Together, our findings reveal the spatial organization of a tumor suppressive immune microenvironment, the mechanisms driving its formation, and its corresponding functionality. This not only strengthens our understanding of tumor immune evasion but provides new targets for immune intervention.

STAR★METHODS

Detailed methods are provided in the online version of this paper and include the following:

SUPPLEMENTAL INFORMATION

Supplemental information can be found online at https://doi.org/10.1016/j.ccell.2024.06.014.

ACKNOWLEDGMENTS

We thank Dr. Ronald N. Germain (National Institutes of Health) and Dr. Hai Qi (Tsinghua University) for providing helpful suggestions and contributing to the manuscript, Dr. Hai Qi for *Ccl22*^{tdTomato} mice, Dr. Ronald N. Germain for *Ubi-tdTomato* mice, Dr. Hongbin Ji (Center for Excellence in Molecular Cell Science, Chinese Academy of Sciences) for KP tumor cell line, Qingfeng Liu, Xiaohong Ma, and Xiufeng Sun in Core facility of biomedical sciences of Xiamen University for confocal and flow cytometry technical support, Jianfeng Wu and Suqin Wu in Laboratory Animal Center of Xiamen University for experimental animal management and *in vitro* fertilization service. This work was supported by the National Key R&D Program of China (2020YFA0803500 to J.H. and K.M., 2023YFC2306400 to H.H.), National Natural Science Foundation of China (81971557 and 32270953 to K.M., 32270928 to H.H.), National Natural Science Foundation of China Major Research Program Integration Project (92042305 to K.M.), the Natural Science Foundation of Fujian Province of China (2021J06004 to K.M.), and the Fundamental Research Funds for the Central Universities of China-Xiamen University (20720210001 to K.M., 20720220003 to K.M., 20720210111 to K.M., and 20720200102 to W.L.).

AUTHOR CONTRIBUTIONS

K.M. conceived this study, generated hypotheses. S.Y. and S.L. performed most experiments and analyzed data. L.Z performed the immunofluorescence imaging of clinical samples. J.R. and H.X. provided the clinical samples. Y.Z. performed parts of mouse tumor immunofluorescence imaging. W. Li. and H.L. helped with cell isolation and sorting. H.N. helped with single cell library construction. C.L. helped with single cell analysis. J.S. and M.T. helped with spatial transcriptomic data analysis and survival analysis. Z.L. and H.H. helped with TCR-sequence and data processing. J. Huang provided the high-performance server system. R.Y. and X.X. helped with cell segmentation and analysis of images. W.D. performed micro scale RNA extraction. W. Lin is responsible for the management of experimental animals. H.H., N.X., J. Han, and S-C.C contributed to data interpretation. K.M., S.Y., and S.L. wrote the manuscript. K.M. supervised the project.

DECLARATION OF INTERESTS

The authors declare no competing interests.

Received: October 2, 2023
Revised: April 29, 2024
Accepted: June 23, 2024
Published: July 18, 2024

REFERENCES

1. Binnewies, M., Roberts, E.W., Kersten, K., Chan, V., Fearon, D.F., Merad, M., Coussens, L.M., Gabrilovich, D.I., Ostrand-Rosenberg, S., Hedrick, C.C., et al. (2018). Understanding the tumor immune microenvironment (TIME) for effective therapy. Nat. Med. *24*, 541–550. https://doi.org/10.1038/s41591-018-0014-x.
2. Salmon, H., Remark, R., Gnjatic, S., and Merad, M. (2019). Host tissue determinants of tumour immunity. Nat. Rev. Cancer *19*, 215–227. https://doi.org/10.1038/s41568-019-0125-9.
3. Ren, X., Zhang, L., Zhang, Y., Li, Z., Siemers, N., and Zhang, Z. (2021). Insights Gained from Single-Cell Analysis of Immune Cells in the Tumor Microenvironment. Annu. Rev. Immunol. *39*, 583–609. https://doi.org/10.1146/annurev-immunol-110519-071134.

4. Jackson, H.W., Fischer, J.R., Zanotelli, V.R.T., Ali, H.R., Mechera, R., Soysal, S.D., Moch, H., Muenst, S., Varga, Z., Weber, W.P., and Bodenmiller, B. (2020). The single-cell pathology landscape of breast cancer. Nature *578*, 615–620. https://doi.org/10.1038/s41586-019-1876-x.

5. Zilionis, R., Engblom, C., Pfirschke, C., Savova, V., Zemmour, D., Saatcioglu, H.D., Krishnan, I., Maroni, G., Meyerovitz, C.V., Kerwin, C.M., et al. (2019). Single-Cell Transcriptomics of Human and Mouse Lung Cancers Reveals Conserved Myeloid Populations across Individuals and Species. Immunity *50*, 1317–1334.e10. https://doi.org/10.1016/j.immuni.2019.03.009.

6. Sautes-Fridman, C., Petitprez, F., Calderaro, J., and Fridman, W.H. (2019). Tertiary lymphoid structures in the era of cancer immunotherapy. Nat. Rev. Cancer *19*, 307–325. https://doi.org/10.1038/s41568-019-0144-6.

7. Risom, T., Glass, D.R., Averbukh, I., Liu, C.C., Baranski, A., Kagel, A., McCaffrey, E.F., Greenwald, N.F., Rivero-Gutiérrez, B., Strand, S.H., et al. (2022). Transition to invasive breast cancer is associated with progressive changes in the structure and composition of tumor stroma. Cell *185*, 299–310.e18. https://doi.org/10.1016/j.cell.2021.12.023.

8. Danenberg, E., Bardwell, H., Zanotelli, V.R.T., Provenzano, E., Chin, S.F., Rueda, O.M., Green, A., Rakha, E., Aparicio, S., Ellis, I.O., et al. (2022). Breast tumor microenvironment structures are associated with genomic features and clinical outcome. Nat. Genet. *54*, 660–669. https://doi.org/10.1038/s41588-022-01041-y.

9. Sorin, M., Rezanejad, M., Karimi, E., Fiset, B., Desharnais, L., Perus, L.J.M., Milette, S., Yu, M.W., Maritan, S.M., Doré, S., et al. (2023). Single-cell spatial landscapes of the lung tumour immune microenvironment. Nature *614*, 548–554. https://doi.org/10.1038/s41586-022-05672-3.

10. Karimi, E., Yu, M.W., Maritan, S.M., Perus, L.J.M., Rezanejad, M., Sorin, M., Dankner, M., Fallah, P., Doré, S., Zuo, D., et al. (2023). Single-cell spatial immune landscapes of primary and metastatic brain tumours. Nature *614*, 555–563. https://doi.org/10.1038/s41586-022-05680-3.

11. Keren, L., Bosse, M., Marquez, D., Angoshtari, R., Jain, S., Varma, S., Yang, S.R., Kurian, A., Van Valen, D., West, R., et al. (2018). A Structured Tumor-Immune Microenvironment in Triple Negative Breast Cancer Revealed by Multiplexed Ion Beam Imaging. Cell *174*, 1373–1387.e19. https://doi.org/10.1016/j.cell.2018.08.039.

12. Wing, J.B., Tanaka, A., and Sakaguchi, S. (2019). Human FOXP3(+) Regulatory T Cell Heterogeneity and Function in Autoimmunity and Cancer. Immunity *50*, 302–316. https://doi.org/10.1016/j.immuni.2019.01.020.

13. Dikiy, S., and Rudensky, A.Y. (2023). Principles of regulatory T cell function. Immunity *56*, 240–255. https://doi.org/10.1016/j.immuni.2023.01.004.

14. Tay, C., Tanaka, A., and Sakaguchi, S. (2023). Tumor-infiltrating regulatory T cells as targets of cancer immunotherapy. Cancer Cell *41*, 450–465. https://doi.org/10.1016/j.ccell.2023.02.014.

15. Plitas, G., and Rudensky, A.Y. (2020). Regulatory T Cells in Cancer. Annu. Rev. Cancer Biol. *4*, 459–477. https://doi.org/10.1146/annurev-cancerbio-030419-033428.

16. Liu, Z., Gerner, M.Y., Van Panhuys, N., Levine, A.G., Rudensky, A.Y., and Germain, R.N. (2015). Immune homeostasis enforced by co-localized effector and regulatory T cells. Nature *528*, 225–230. https://doi.org/10.1038/nature16169.

17. Wong, H.S., Park, K., Gola, A., Baptista, A.P., Miller, C.H., Deep, D., Lou, M., Boyd, L.F., Rudensky, A.Y., Savage, P.A., et al. (2021). A local regulatory T cell feedback circuit maintains immune homeostasis by pruning self-activated T cells. Cell *184*, 3981–3997.e22. https://doi.org/10.1016/j.cell.2021.05.028.

18. Levine, A.G., Arvey, A., Jin, W., and Rudensky, A.Y. (2014). Continuous requirement for the TCR in regulatory T cell function. Nat. Immunol. *15*, 1070–1078. https://doi.org/10.1038/ni.3004.

19. Vahl, J.C., Drees, C., Heger, K., Heink, S., Fischer, J.C., Nedjic, J., Ohkura, N., Morikawa, H., Poeck, H., Schallenberg, S., et al. (2014). Continuous T cell receptor signals maintain a functional regulatory T cell pool. Immunity *41*, 722–736. https://doi.org/10.1016/j.immuni.2014.10.012.

20. De Simone, M., Arrigoni, A., Rossetti, G., Gruarin, P., Ranzani, V., Politano, C., Bonnal, R.J.P., Provasi, E., Sarnicola, M.L., Panzeri, I., et al. (2016). Transcriptional Landscape of Human Tissue Lymphocytes Unveils Uniqueness of Tumor-Infiltrating T Regulatory Cells. Immunity *45*, 1135–1147. https://doi.org/10.1016/j.immuni.2016.10.021.

21. Guo, X., Zhang, Y., Zheng, L., Zheng, C., Song, J., Zhang, Q., Kang, B., Liu, Z., Jin, L., Xing, R., et al. (2018). Global characterization of T cells in non-small-cell lung cancer by single-cell sequencing. Nat. Med. *24*, 978–985. https://doi.org/10.1038/s41591-018-0045-3.

22. Plitas, G., Konopacki, C., Wu, K., Bos, P.D., Morrow, M., Putintseva, E.V., Chudakov, D.M., and Rudensky, A.Y. (2016). Regulatory T Cells Exhibit Distinct Features in Human Breast Cancer. Immunity *45*, 1122–1134. https://doi.org/10.1016/j.immuni.2016.10.032.

23. Fu, J., Xu, D., Liu, Z., Shi, M., Zhao, P., Fu, B., Zhang, Z., Yang, H., Zhang, H., Zhou, C., et al. (2007). Increased regulatory T cells correlate with CD8 T-cell impairment and poor survival in hepatocellular carcinoma patients. Gastroenterology *132*, 2328–2339. https://doi.org/10.1053/j.gastro.2007.03.102.

24. Shen, Z., Zhou, S., Wang, Y., Li, R.L., Zhong, C., Liang, C., and Sun, Y. (2010). Higher intratumoral infiltrated Foxp3+ Treg numbers and Foxp3+/CD8+ ratio are associated with adverse prognosis in resectable gastric cancer. J. Cancer Res. Clin. Oncol. *136*, 1585–1595. https://doi.org/10.1007/s00432-010-0816-9.

25. Petersen, R.P., Campa, M.J., Sperlazza, J., Conlon, D., Joshi, M.B., Harpole, D.H., Jr., and Patz, E.F., Jr. (2006). Tumor infiltrating Foxp3+ regulatory T-cells are associated with recurrence in pathologic stage I NSCLC patients. Cancer *107*, 2866–2872. https://doi.org/10.1002/cncr.22282.

26. Watson, M.J., Vignali, P.D.A., Mullett, S.J., Overacre-Delgoffe, A.E., Peralta, R.M., Grebinoski, S., Menk, A.V., Rittenhouse, N.L., DePeaux, K., Whetstone, R.D., et al. (2021). Metabolic support of tumour-infiltrating regulatory T cells by lactic acid. Nature *591*, 645–651. https://doi.org/10.1038/s41586-020-03045-2.

27. Kumagai, S., Koyama, S., Itahashi, K., Tanegashima, T., Lin, Y.T., Togashi, Y., Kamada, T., Irie, T., Okumura, G., Kono, H., et al. (2022). Lactic acid promotes PD-1 expression in regulatory T cells in highly glycolytic tumor microenvironments. Cancer Cell *40*, 201–218.e9. https://doi.org/10.1016/j.ccell.2022.01.001.

28. Wang, H., Franco, F., Tsui, Y.C., Xie, X., Trefny, M.P., Zappasodi, R., Mohmood, S.R., Fernández-García, J., Tsai, C.H., Schulze, I., et al. (2020). CD36-mediated metabolic adaptation supports regulatory T cell survival and function in tumors. Nat. Immunol. *21*, 298–308. https://doi.org/10.1038/s41590-019-0589-5.

29. Angelin, A., Gil-de-Gomez, L., Dahiya, S., Jiao, J., Guo, L., Levine, M.H., Wang, Z., Quinn, W.J., 3rd, Kopinski, P.K., Wang, L., et al. (2017). Foxp3 Reprograms T Cell Metabolism to Function in Low-Glucose, High-Lactate Environments. Cell Metab. *25*, 1282–1293.e7. https://doi.org/10.1016/j.cmet.2016.12.018.

30. Moreno Ayala, M.A., Campbell, T.F., Zhang, C., Dahan, N., Bockman, A., Prakash, V., Feng, L., Sher, T., and DuPage, M. (2023). CXCR3 expression in regulatory T cells drives interactions with type I dendritic cells in tumors to restrict CD8(+) T cell antitumor immunity. Immunity *56*, 1613–1630.e5. https://doi.org/10.1016/j.immuni.2023.06.003.

31. Egen, J.G., Ouyang, W., and Wu, L.C. (2020). Human Anti-tumor Immunity: Insights from Immunotherapy Clinical Trials. Immunity *52*, 36–54. https://doi.org/10.1016/j.immuni.2019.12.010.

32. Hiam-Galvez, K.J., Allen, B.M., and Spitzer, M.H. (2021). Systemic immunity in cancer. Nat. Rev. Cancer *21*, 345–359. https://doi.org/10.1038/s41568-021-00347-z.

33. Fuertes, M.B., Kacha, A.K., Kline, J., Woo, S.R., Kranz, D.M., Murphy, K.M., and Gajewski, T.F. (2011). Host type I IFN signals are required for antitumor CD8+ T cell responses through CD8{alpha}+ dendritic cells. J. Exp. Med. *208*, 2005–2016. https://doi.org/10.1084/jem.20101159.

34. Broz, M.L., Binnewies, M., Boldajipour, B., Nelson, A.E., Pollack, J.L., Erle, D.J., Barczak, A., Rosenblum, M.D., Daud, A., Barber, D.L., et al. (2014). Dissecting the tumor myeloid compartment reveals rare activating antigen-presenting cells critical for T cell immunity. Cancer Cell *26*, 638–652. https://doi.org/10.1016/j.ccell.2014.09.007.

35. Spranger, S., Dai, D., Horton, B., and Gajewski, T.F. (2017). Tumor-Residing Batf3 Dendritic Cells Are Required for Effector T Cell Trafficking and Adoptive T Cell Therapy. Cancer Cell *31*, 711–723.e4. https://doi.org/10.1016/j.ccell.2017.04.003.

36. Bottcher, J.P., Bonavita, E., Chakravarty, P., Blees, H., Cabeza-Cabrerizo, M., Sammicheli, S., Rogers, N.C., Sahai, E., Zelenay, S., and Reis e Sousa, C. (2018). NK Cells Stimulate Recruitment of cDC1 into the Tumor Microenvironment Promoting Cancer Immune Control. Cell *172*, 1022–1037.e14. https://doi.org/10.1016/j.cell.2018.01.004.

37. Duong, E., Fessenden, T.B., Lutz, E., Dinter, T., Yim, L., Blatt, S., Bhutkar, A., Wittrup, K.D., and Spranger, S. (2022). Type I interferon activates MHC class I-dressed CD11b(+) conventional dendritic cells to promote protective anti-tumor CD8(+) T cell immunity. Immunity *55*, 308–323.e9. https://doi.org/10.1016/j.immuni.2021.10.020.

38. Zhang, Q., He, Y., Luo, N., Patel, S.J., Han, Y., Gao, R., Modak, M., Carotta, S., Haslinger, C., Kind, D., et al. (2019). Landscape and Dynamics of Single Immune Cells in Hepatocellular Carcinoma. Cell *179*, 829–845.e20. https://doi.org/10.1016/j.cell.2019.10.003.

39. Maier, B., Leader, A.M., Chen, S.T., Tung, N., Chang, C., LeBerichel, J., Chudnovskiy, A., Maskey, S., Walker, L., Finnigan, J.P., et al. (2020). A conserved dendritic-cell regulatory program limits antitumour immunity. Nature *580*, 257–262. https://doi.org/10.1038/s41586-020-2134-y.

40. Zhang, L., Li, Z., Skrzypczynska, K.M., Fang, Q., Zhang, W., O'Brien, S.A., He, Y., Wang, L., Zhang, Q., Kim, A., et al. (2020). Single-Cell Analyses Inform Mechanisms of Myeloid-Targeted Therapies in Colon Cancer. Cell *181*, 442–459.e29. https://doi.org/10.1016/j.cell.2020.03.048.

41. Cheng, S., Li, Z., Gao, R., Xing, B., Gao, Y., Yang, Y., Qin, S., Zhang, L., Ouyang, H., Du, P., et al. (2021). A pan-cancer single-cell transcriptional atlas of tumor infiltrating myeloid cells. Cell *184*, 792–809.e23. https://doi.org/10.1016/j.cell.2021.01.010.

42. Di Pilato, M., Kfuri-Rubens, R., Pruessmann, J.N., Ozga, A.J., Messemaker, M., Cadilha, B.L., Sivakumar, R., Cianciaruso, C., Warner, R.D., Marangoni, F., et al. (2021). CXCR6 positions cytotoxic T cells to receive critical survival signals in the tumor microenvironment. Cell *184*, 4512–4530.e22. https://doi.org/10.1016/j.cell.2021.07.015.

43. Moser, A.R., Luongo, C., Gould, K.A., McNeley, M.K., Shoemaker, A.R., and Dove, W.F. (1995). ApcMin: a mouse model for intestinal and mammary tumorigenesis. Eur. J. Cancer *31A*, 1061–1064. https://doi.org/10.1016/0959-8049(95)00181-h.

44. Moser, A.R., Pitot, H.C., and Dove, W.F. (1990). A dominant mutation that predisposes to multiple intestinal neoplasia in the mouse. Science *247*, 322–324. https://doi.org/10.1126/science.2296722.

45. Cancer Genome Atlas Network (2012). Comprehensive molecular characterization of human colon and rectal cancer. Nature *487*, 330–337. https://doi.org/10.1038/nature11252.

46. Piyadasa, H., Angelo, M., and Bendall, S.C. (2023). Spatial proteomics of tumor microenvironments reveal why location matters. Nat. Immunol. *24*, 565–566. https://doi.org/10.1038/s41590-023-01471-8.

47. Gerner, M.Y., Kastenmuller, W., Ifrim, I., Kabat, J., and Germain, R.N. (2012). Histo-cytometry: a method for highly multiplex quantitative tissue imaging analysis applied to dendritic cell subset microanatomy in lymph nodes. Immunity *37*, 364–376. https://doi.org/10.1016/j.immuni.2012.07.011.

48. Li, W., Germain, R.N., and Gerner, M.Y. (2019). High-dimensional cell-level analysis of tissues with Ce3D multiplex volume imaging. Nat. Protoc. *14*, 1708–1733. https://doi.org/10.1038/s41596-019-0156-4.

49. Ruoslahti, E. (2002). Specialization of tumour vasculature. Nat. Rev. Cancer *2*, 83–90. https://doi.org/10.1038/nrc724.

50. Schaaf, M.B., Garg, A.D., and Agostinis, P. (2018). Defining the role of the tumor vasculature in antitumor immunity and immunotherapy. Cell Death Dis. *9*, 115. https://doi.org/10.1038/s41419-017-0061-0.

51. Robanus-Maandag, E.C., Koelink, P.J., Breukel, C., Salvatori, D.C.F., Jagmohan-Changur, S.C., Bosch, C.A.J., Verspaget, H.W., Devilee, P., Fodde, R., and Smits, R. (2010). A new conditional Apc-mutant mouse model for colorectal cancer. Carcinogenesis *31*, 946–952. https://doi.org/10.1093/carcin/bgq046.

52. Dzutsev, A., Badger, J.H., Perez-Chanona, E., Roy, S., Salcedo, R., Smith, C.K., and Trinchieri, G. (2017). Microbes and Cancer. Annu. Rev. Immunol. *35*, 199–228. https://doi.org/10.1146/annurev-immunol-051116-052133.

53. Brennan, C.A., and Garrett, W.S. (2016). Gut Microbiota, Inflammation, and Colorectal Cancer. Annu. Rev. Microbiol. *70*, 395–411. https://doi.org/10.1146/annurev-micro-102215-095513.

54. Hanzelmann, S., Castelo, R., and Guinney, J. (2013). GSVA: gene set variation analysis for microarray and RNA-seq data. BMC Bioinf. *14*, 7. https://doi.org/10.1186/1471-2105-14-7.

55. Efremova, M., Vento-Tormo, M., Teichmann, S.A., and Vento-Tormo, R. (2020). CellPhoneDB: inferring cell-cell communication from combined expression of multi-subunit ligand-receptor complexes. Nat. Protoc. *15*, 1484–1506. https://doi.org/10.1038/s41596-020-0292-x.

56. Liu, B., Lin, Y., Yan, J., Yao, J., Liu, D., Ma, W., Wang, J., Liu, W., Wang, C., Zhang, L., and Qi, H. (2021). Affinity-coupled CCL22 promotes positive selection in germinal centres. Nature *592*, 133–137. https://doi.org/10.1038/s41586-021-03239-2.

57. Curiel, T.J., Coukos, G., Zou, L., Alvarez, X., Cheng, P., Mottram, P., Evdemon-Hogan, M., Conejo-Garcia, J.R., Zhang, L., Burow, M., et al. (2004). Specific recruitment of regulatory T cells in ovarian carcinoma fosters immune privilege and predicts reduced survival. Nat. Med. *10*, 942–949. https://doi.org/10.1038/nm1093.

58. Chen, J., Zhao, D., Zhang, L., Zhang, J., Xiao, Y., Wu, Q., Wang, Y., and Zhan, Q. (2022). Tumor-associated macrophage (TAM)-derived CCL22 induces FAK addiction in esophageal squamous cell carcinoma (ESCC). Cell. Mol. Immunol. *19*, 1054–1066. https://doi.org/10.1038/s41423-022-00903-z.

59. Fu, T., Dai, L.J., Wu, S.Y., Xiao, Y., Ma, D., Jiang, Y.Z., and Shao, Z.M. (2021). Spatial architecture of the immune microenvironment orchestrates tumor immunity and therapeutic response. J. Hematol. Oncol. *14*, 98. https://doi.org/10.1186/s13045-021-01103-4.

60. Moran, A.E., Holzapfel, K.L., Xing, Y., Cunningham, N.R., Maltzman, J.S., Punt, J., and Hogquist, K.A. (2011). T cell receptor signal strength in Treg and iNKT cell development demonstrated by a novel fluorescent reporter mouse. J. Exp. Med. *208*, 1279–1289. https://doi.org/10.1084/jem.20110308.

61. Pere, H., Montier, Y., Bayry, J., Quintin-Colonna, F., Merillon, N., Dransart, E., Badoual, C., Gey, A., Ravel, P., Marcheteau, E., et al. (2011). A CCR4 antagonist combined with vaccines induces antigen-specific CD8+ T cells and tumor immunity against self antigens. Blood *118*, 4853–4862. https://doi.org/10.1182/blood-2011-01-329656.

62. Bayry, J., Tchilian, E.Z., Davies, M.N., Forbes, E.K., Draper, S.J., Kaveri, S.V., Hill, A.V.S., Kazatchkine, M.D., Beverley, P.C.L., Flower, D.R., and Tough, D.F. (2008). In silico identified CCR4 antagonists target regulatory T cells and exert adjuvant activity in vaccination. Proc. Natl. Acad. Sci. USA *105*, 10221–10226. https://doi.org/10.1073/pnas.0803453105.

63. van Pul, K.M., Fransen, M.F., van de Ven, R., and de Gruijl, T.D. (2021). Immunotherapy Goes Local: The Central Role of Lymph Nodes in Driving Tumor Infiltration and Efficacy. Front. Immunol. *12*, 643291. https://doi.org/10.3389/fimmu.2021.643291.

64. du Bois, H., Heim, T.A., and Lund, A.W. (2021). Tumor-draining lymph nodes: At the crossroads of metastasis and immunity. Sci. Immunol. *6*, eabg3551. https://doi.org/10.1126/sciimmunol.abg3551.

65. Roberts, E.W., Broz, M.L., Binnewies, M., Headley, M.B., Nelson, A.E., Wolf, D.M., Kaisho, T., Bogunovic, D., Bhardwaj, N., and Krummel, M.F. (2016). Critical Role for CD103(+)/CD141(+) Dendritic Cells Bearing CCR7 for Tumor Antigen Trafficking and Priming of T Cell Immunity in

Melanoma. Cancer Cell *30*, 324–336. https://doi.org/10.1016/j.ccell.2016.06.003.

66. Zagorulya, M., Yim, L., Morgan, D.M., Edwards, A., Torres-Mejia, E., Momin, N., McCreery, C.V., Zamora, I.L., Horton, B.L., Fox, J.G., et al. (2023). Tissue-specific abundance of interferon-gamma drives regulatory T cells to restrain DC1-mediated priming of cytotoxic T cells against lung cancer. Immunity *56*, 386–405.e10. https://doi.org/10.1016/j.immuni.2023.01.010.

67. Park, K., Mikulski, Z., Seo, G.Y., Andreyev, A.Y., Marcovecchio, P., Blatchley, A., Kronenberg, M., and Hedrick, C.C. (2016). The transcription factor NR4A3 controls CD103+ dendritic cell migration. J. Clin. Invest. *126*, 4603–4615. https://doi.org/10.1172/JCI87081.

68. Satpathy, A.T., Briseño, C.G., Lee, J.S., Ng, D., Manieri, N.A., Kc, W., Wu, X., Thomas, S.R., Lee, W.L., Turkoz, M., et al. (2013). Notch2-dependent classical dendritic cells orchestrate intestinal immunity to attaching-and-effacing bacterial pathogens. Nat. Immunol. *14*, 937–948. https://doi.org/10.1038/ni.2679.

69. Valdeolivas, A., Amberg, B., Giroud, N., Richardson, M., Gálvez, E.J.C., Badillo, S., Julien-Laferrière, A., Túrós, D., Voith von Voithenberg, L., Wells, I., et al. (2024). Profiling the heterogeneity of colorectal cancer consensus molecular subtypes using spatial transcriptomics. npj Precis. Oncol. *8*, 10. https://doi.org/10.1038/s41698-023-00488-4.

70. Di Palma, S., and Bodenmiller, B. (2015). Unraveling cell populations in tumors by single-cell mass cytometry. Curr. Opin. Biotechnol. *31*, 122–129. https://doi.org/10.1016/j.copbio.2014.07.004.

71. Dykema, A.G., Zhang, J., Cheung, L.S., Connor, S., Zhang, B., Zeng, Z., Cherry, C.M., Li, T., Caushi, J.X., Nishimoto, M., et al. (2023). Lung tumor-infiltrating T(reg) have divergent transcriptional profiles and function linked to checkpoint blockade response. Sci. Immunol. *8*, eadg1487. https://doi.org/10.1126/sciimmunol.adg1487.

72. Binnewies, M., Mujal, A.M., Pollack, J.L., Combes, A.J., Hardison, E.A., Barry, K.C., Tsui, J., Ruhland, M.K., Kersten, K., Abushawish, M.A., et al. (2019). Unleashing Type-2 Dendritic Cells to Drive Protective Antitumor CD4(+) T Cell Immunity. Cell *177*, 556–571.e16. https://doi.org/10.1016/j.cell.2019.02.005.

73. Li, J., Zhou, J., Huang, H., Jiang, J., Zhang, T., and Ni, C. (2023). Mature dendritic cells enriched in immunoregulatory molecules (mregDCs): A novel population in the tumour microenvironment and immunotherapy target. Clin. Transl. Med. *13*, e1199. https://doi.org/10.1002/ctm2.1199.

74. Ginhoux, F., Guilliams, M., and Merad, M. (2022). Expanding dendritic cell nomenclature in the single-cell era. Nat. Rev. Immunol. *22*, 67–68. https://doi.org/10.1038/s41577-022-00675-7.

75. Meiser, P., Knolle, M.A., Hirschberger, A., de Almeida, G.P., Bayerl, F., Lacher, S., Pedde, A.M., Flommersfeld, S., Hönninger, J., Stark, L., et al. (2023). A distinct stimulatory cDC1 subpopulation amplifies CD8(+) T cell responses in tumors for protective anti-cancer immunity. Cancer Cell *41*, 1498–1515.e10. https://doi.org/10.1016/j.ccell.2023.06.008.

76. Kastenmuller, W., Brandes, M., Wang, Z., Herz, J., Egen, J.G., and Germain, R.N. (2013). Peripheral prepositioning and local CXCL9 chemokine-mediated guidance orchestrate rapid memory CD8+ T cell responses in the lymph node. Immunity *38*, 502–513. https://doi.org/10.1016/j.immuni.2012.11.012.

77. Han, X., Li, F., Fang, Z., Gao, Y., Li, F., Fang, R., Yao, S., Sun, Y., Li, L., Zhang, W., et al. (2014). Transdifferentiation of lung adenocarcinoma in mice with Lkb1 deficiency to squamous cell carcinoma. Nat. Commun. *5*, 3261. https://doi.org/10.1038/ncomms4261.

78. Mao, K., Baptista, A.P., Tamoutounour, S., Zhuang, L., Bouladoux, N., Martins, A.J., Huang, Y., Gerner, M.Y., Belkaid, Y., and Germain, R.N. (2018). Innate and adaptive lymphocytes sequentially shape the gut microbiota and lipid metabolism. Nature *554*, 255–259. https://doi.org/10.1038/nature25437.

79. McQuin, C., Goodman, A., Chernyshev, V., Kamentsky, L., Cimini, B.A., Karhohs, K.W., Doan, M., Ding, L., Rafelski, S.M., Thirstrup, D., et al. (2018). CellProfiler 3.0: Next-generation image processing for biology. PLoS Biol. *16*, e2005970. https://doi.org/10.1371/journal.pbio.2005970.

80. Picelli, S., Faridani, O.R., Björklund, A.K., Winberg, G., Sagasser, S., and Sandberg, R. (2014). Full-length RNA-seq from single cells using Smart-seq2. Nat. Protoc. *9*, 171–181. https://doi.org/10.1038/nprot.2014.006.

81. Bolotin, D.A., Poslavsky, S., Mitrophanov, I., Shugay, M., Mamedov, I.Z., Putintseva, E.V., and Chudakov, D.M. (2015). MiXCR: software for comprehensive adaptive immunity profiling. Nat. Methods *12*, 380–381. https://doi.org/10.1038/nmeth.3364.

82. Korsunsky, I., Millard, N., Fan, J., Slowikowski, K., Zhang, F., Wei, K., Baglaenko, Y., Brenner, M., Loh, P.R., and Raychaudhuri, S. (2019). Fast, sensitive and accurate integration of single-cell data with Harmony. Nat. Methods *16*, 1289–1296. https://doi.org/10.1038/s41592-019-0619-0.

83. Alshetaiwi, H., Pervolarakis, N., McIntyre, L.L., Ma, D., Nguyen, Q., Rath, J.A., Nee, K., Hernandez, G., Evans, K., Torosian, L., et al. (2020). Defining the emergence of myeloid-derived suppressor cells in breast cancer using single-cell transcriptomics. Sci. Immunol. *5*, eaay6017. https://doi.org/10.1126/sciimmunol.aay6017.

84. Garcia-Alonso, L., Handfield, L.F., Roberts, K., Nikolakopoulou, K., Fernando, R.C., Gardner, L., Woodhams, B., Arutyunyan, A., Polanski, K., Hoo, R., et al. (2021). Mapping the temporal and spatial dynamics of the human endometrium *in vivo* and *in vitro*. Nat. Genet. *53*, 1698–1711. https://doi.org/10.1038/s41588-021-00972-2.

85. Webster, K.E., Walters, S., Kohler, R.E., Mrkvan, T., Boyman, O., Surh, C.D., Grey, S.T., and Sprent, J. (2009). In vivo expansion of T reg cells with IL-2-mAb complexes: induction of resistance to EAE and long-term acceptance of islet allografts without immunosuppression. J. Exp. Med. *206*, 751–760. https://doi.org/10.1084/jem.20082824.

86. Hao, Y., Hao, S., Andersen-Nissen, E., Mauck, W.M., 3rd, Zheng, S., Butler, A., Lee, M.J., Wilk, A.J., Darby, C., Zager, M., et al. (2021). Integrated analysis of multimodal single-cell data. Cell *184*, 3573–3587.e29. https://doi.org/10.1016/j.cell.2021.04.048.

87. Colaprico, A., Silva, T.C., Olsen, C., Garofano, L., Cava, C., Garolini, D., Sabedot, T.S., Malta, T.M., Pagnotta, S.M., Castiglioni, I., et al. (2016). TCGAbiolinks: an R/Bioconductor package for integrative analysis of TCGA data. Nucleic Acids Res. *44*, e71. https://doi.org/10.1093/nar/gkv1507.

STAR★METHODS

KEY RESOURCES TABLE

REAGENT or RESOURCE	SOURCE	IDENTIFIER
Antibodies		
BV480 rat anti-mouse CD3 Molecular Complex (Clone 17A2)	BD Biosciences	Cat# 565642; RRID: AB_2739318
Alexa Fluor® 488 anti-mouse CD3 Antibody (Clone 17A2)	BioLegend	Cat# 100210; RRID: AB_389301
eFluor 570 anti-mouse CD45R (B220) Monoclonal Antibody (Clone RA3-6B2)	eBioscience™	Cat# 41-0452-80; RRID: AB_2573598
Alexa Fluor® 488 anti-mouse CD11c Antibody (Clone N418)	BioLegend	Cat# 117311; RRID: AB_389306
Alexa Fluor® 647 anti-mouse CD11c Antibody (Clone N418)	BioLegend	Cat# 117312; RRID: AB_389328
Alexa Fluor® 488 anti-mouse CD31 Antibody (Clone MEC13.3)	BioLegend	Cat# 102513; RRID: AB_493413
BV480 rat anti-mouse CD4 (Clone RM4-5)	BD Biosciences	Cat# 565634; RRID: AB_2739312
Alexa Fluor® 488 rat anti-mouse CD4 (Clone RM4-5)	BD Biosciences	Cat# 557667; RRID: AB_396779
BV480 rat anti-mouse CD8a (Clone 53-6.7)	BD Biosciences	Cat# 566096; RRID: AB_2739500
Alexa Fluor® 594 anti-mouse CD8a Antibody (Clone 53-6.7)	BioLegend	Cat# 100758; RRID: AB_2563237
eFluor 450 anti-mouse CD326 (EpCAM) Monoclonal Antibody (Clone G8.8)	eBioscience™	Cat# 48-5791-82; RRID: AB_10717090
Alexa Fluor® 594 anti-mouse CD326 (EpCAM) Antibody (Clone G8.8)	BioLegend	Cat# 118222; RRID: AB_2563322
Alexa Fluor 488 anti-mouse F4/80 Monoclonal Antibody (Clone BM8)	eBioscience™	Cat# 53-4801-82; RRID: AB_469915
CD11b Monoclonal Antibody, eFluor™ 450 (Clone M1/70)	eBioscience™	Cat# 48-0112-82; RRID: AB_1582236
Mouse Integrin alpha E/CD103 Antibody	R&D Systems	Cat# AF1990; RRID: AB_2128618
Alexa Fluor 488 anti-mouse Foxp3 Monoclonal Antibody (Clone FJK-16s)	eBioscience™	Cat# 53-5773-82; RRID: AB_763537
eFluor 570 anti-mouse Foxp3 Monoclonal Antibody (Clone FJK-16s)	eBioscience™	Cat# 41-5773-82; RRID: AB_11219073
eFluor 660 anti-mouse Foxp3 Monoclonal Antibody (Clone FJK-16s)	eBioscience™	Cat# 50-5773-82; RRID: AB_11218868
Alexa Fluor® 488 anti-GFP (Clone FM264G)	BioLegend	Cat# 338008; RRID: AB_2563288
Alexa Fluor® 647 mouse anti-Ki-67 (Clone B56)	BD Biosciences	Cat# 561126; RRID: AB_10611874
Alexa Fluor® 700 mouse anti-Ki-67 (Clone B56)	BD Biosciences	Cat# 561277; RRID: AB_10611571
Alexa Fluor 488 anti-mouse LYVE1 monoclonal antibody (Clone ALY7)	eBioscience™	Cat# 53-0443-82; RRID: AB_1633415
eFluor 450 anti-mouse LYVE1 Monoclonal Antibody (Clone ALY7)	eBioscience™	Cat# 48-0443-80; RRID: AB_2784722
eFluor 660 anti-mouse LYVE1 Monoclonal Antibody (Clone ALY7)	eBioscience™	Cat# 50-0443-82; RRID: AB_10597449
Alexa Fluor® 488 anti-mouse I-A/I-E Antibody (Clone M5/114.15.2)	BioLegend	Cat# 107616; RRID: AB_493523
Alexa Fluor 700 anti-mouse MHC Class II (I-A/I-E) Monoclonal Antibody (Clone M5/114.15.2)	eBioscience™	Cat# 56-5321-80; RRID: AB_494010

(*Continued on next page*)

Continued

REAGENT or RESOURCE	SOURCE	IDENTIFIER
Purified anti-mouse CD279 (PD-1) Antibody (Clone RMP1-30)	BioLegend	Cat# 109101; RRID: AB_313418
Alexa Fluor® 647 anti-mouse CD279 (PD-1) Antibody (Clone RMP1-30)	BioLegend	Cat# 109118; RRID: AB_2566550
Recombinant Anti-OX40 Antibody (Clone EPR22229-5)	Abcam	Cat# ab229021; RRID: AB_3065191
Mouse CCL21/6Ckine Antibody	R&D Systems	Cat# AF457; RRID: AB_2072083
Alexa Fluor® 488 anti-human CD3 Antibody (Clone UCHT1)	BioLegend	Cat# 300454; RRID: AB_2564149
BV480 Mouse Anti-Human CD4 (Clone RPA-T4)	BD Biosciences	Cat# 746541; RRID: AB_2743832
Alexa Fluor® 594 anti-human Podoplanin Antibody (Clone NC-08)	BioLegend	Cat# 337018; RRID: AB_2629590
Anti-LYVE1 antibody	Abcam	Cat# ab10278; RRID: AB_297016
FOXP3 Monoclonal Antibody, eFluor 570 (Clone 236A/E7)	eBioscience™	Cat# 2221059; RRID: AB_2573609
Hoechst 33342, trihydrochloride, trihydrate *FluoroPure™ grade*	Thermo Fischer Scientific	Cat# H21492
Alexa Fluor® 488 Goat Anti-Rat IgG (H+L) Antibody	Life Technologies	Cat# A-11006; RRID: AB_2534074
Donkey anti-Goat IgG (H+L) Cross-Adsorbed Secondary Antibody, Alexa Fluor™ 555	Life Technologies	Cat# A-21432; RRID: AB_2535853
Donkey anti-Rabbit IgG (H+L) Highly Cross-Adsorbed Secondary Antibody, Alexa Fluor™ 488	Life Technologies	Cat# A21206; RRID: AB_2535792
Donkey anti-Rabbit IgG (H+L) Highly Cross-Adsorbed Secondary Antibody, Alexa Fluor™ 594	Life Technologies	Cat# A21207; RRID: AB_141637
Goat anti-Rat IgG (H+L) Cross-Adsorbed Secondary Antibody, Alexa Fluor 647	Life Technologies	Cat# A21247; RRID: AB_141778
Donkey anti-Rat IgG (H+L) Highly Cross-Adsorbed Secondary Antibody, Alexa Fluor™ 647	Life Technologies	Cat# A78947; RRID: AB_2910635
Goat anti-Rabbit IgG (H+L) Highly Cross-Adsorbed Secondary Antibody, Alexa Fluor 488	Life Technologies	Cat# A-11034; RRID: AB_2576217
APC anti-mouse CD45R (B220) Monoclonal Antibody (Clone RA3-6B2)	eBioscience™	Cat# 17-0452-82; RRID: AB_469395
PE anti-mouse CD3 Antibody (Clone 17A2)	BioLegend	Cat# 100206; RRID: AB_469395
APC/Cyanine7 anti-mouse CD3 Antibody (Clone 17A2)	BioLegend	Cat# 100222; RRID: AB_2242784
APC anti-mouse CD11b Monoclonal Antibody (Clone M/70)	eBioscience™	Cat# 17-0112-82; RRID: AB_469343
FITC anti-mouse CD11c Monoclonal Antibody (Clone N418)	eBioscience™	Cat# 11-0114-82; RRID: AB_464940
BV421 anti-mouse CD11c Monoclonal Antibody (Clone HL3)	BD Biosciences	Cat#562782; RRID: AB_2737789
PE-Cyanine7 anti-mouse CD64 Monoclonal Antibody (Clone X54-5/7.1)	BioLegend	Cat# 139314; RRID: AB_2563904
Brilliant Violet 605™ anti-mouse Ly-6C Monoclonal Antibody (Clone HK1.4)	BioLegend	Cat# 128036; RRID: AB_2562353
CD16/32 purified 2.4G2	BD Biosciences	Cat#553142; RRID: AB_394656

(*Continued on next page*)

Continued

REAGENT or RESOURCE	SOURCE	IDENTIFIER
FITC anti-mouse CD25 Monoclonal Antibody (Clone PC61.5.3)	Thermo Fischer Scientific	Cat# MA5-17815; RRID: AB_2539199
PE anti-mouse CD25 Monoclonal Antibody (Clone PC61.5)	eBioscience™	Cat# 12-0251-82; RRID: AB_465607
PE anti-mouse CD278 Monoclonal Antibody (Clone7E.17G9)	eBioscience™	Cat# 12-9942-81; RRID: AB_466273
Brilliant Violet 510™ anti-mouse CD4 Antibody (Clone GK1.5)	BioLegend	Cat# 100449; RRID: AB_2564587
BV421 Rat Anti-Mouse CD45 (Clone 30-F11)	BD Biosciences	Cat# 563890; RRID: AB_2651151
Alexa Fluor 700 Rat Anti-Mouse CD45 (Clone 30-F11)	eBioscience™	Cat# 56-0541-82; RRID: AB_891454
Brilliant Violet 510™ anti-mouse CD45 Antibody (Clone 30-F11)	BioLegend	Cat# 103138; RRID: AB_2563061
BUV395 Rat Anti-Mouse CD45 (Clone 30-F11)	BD Biosciences	Cat# 564279; RRID: AB_2561134
PE anti-mouse CD152 (CTLA-4) Monoclonal Antibody (Clone UC10-4B9)	Thermo Fischer Scientific	Cat# 12-1522-82; RRID: AB_465879
APC anti-mouse TCR β chain Antibody (Clone H57-597)	BioLegend	Cat# 109212; RRID: AB_313435
Alexa Fluor 488 anti-mouse Foxp3 Monoclonal Antibody (Clone FJK-16s)	eBioscience™	Cat# 53-5773-82; RRID: AB_763537
Percp-cyanine5.5 anti-mouse Foxp3 Monoclonal Antibody (Clone FJK-16s)	eBioscience™	Cat# 45-5773-82; RRID: AB_914351
APC anti-mouse Foxp3 Monoclonal Antibody (Clone FJK-16s)	eBioscience™	Cat# 17-5773-82; RRID: AB_469457
APC anti-mouse CD278 (ICOS) Monoclonal Antibody (Clone 7E.17G9)	eBioscience™	Cat# 17-9942-80; RRID: AB_2716947
PE anti-mouse CD366 (TIM-3) Antibody (Clone RMT3-23)	BioLegend	Cat# 119703; RRID: AB_345377
PE/Cyanine7 anti-mouse CD279 (PD-1) Antibody (Clone 29F.1A12)	BioLegend	Cat# 135215; RRID: AB_10696422
Percp-cyanine 5.5 anti-mouse MHC Class II (I-A/I-E) Monoclonal Antibody (Clone M5/114.15.2)	BioLegend	Cat# 107626; RRID: AB_2191071
PE anti-mouse CD134 (OX-40) Monoclonal Antibody (Clone OX-86)	eBioscience™	Cat# 12-1341-81; RRID: AB_465853
Brilliant Violet 421™ anti-mouse CD134 (OX-40) Monoclonal Antibody (Clone OX-86)	BioLegend	Cat# 119411; RRID: AB_10962569
Alexa Fluor® 488 anti-mouse CD103 Antibody (Clone 2E7)	BioLegend	Cat# 121408; RRID: AB_535950
Alexa Fluor® 700 anti-mouse/human CD45R/B220 Antibody (Clone RA3-6B2)	BioLegend	Cat# 103232; RRID: AB_493717
Brilliant Violet 711™ anti-mouse CD64 (FcγRI) Antibody (Clone X54-5/7.1)	BioLegend	Cat# 139311; RRID: AB_2563846
Brilliant Violet 785 anti-mouse CD11b Antibody (Clone M1/70)	BioLegend	Cat# 101243; RRID: AB_2561373
PE/Cyanine7 anti-mouse CD80 Antibody (Clone 16-10A1)	BioLegend	Cat# 104734; RRID: AB_2563113
Brilliant Violet 510 anti-mouse CD86 Antibody (Clone GL-1)	BioLegend	Cat# 105039; RRID: AB_2562370
Brilliant Violet 605 anti-mouse CD197 (CCR7) Antibody (Clone 4B12)	BioLgend	Cat# 120125; RRID: AB_ 2715777

(*Continued on next page*)

Continued

REAGENT or RESOURCE	SOURCE	IDENTIFIER
eBioscience™ Fixable Viability Dye eFluor™ 780	eBioscience™	Cat# 65-0865-14
*InVivo*MAb anti-mouse MHC Class II (I-A/I-E) (Clone M5/114)	BioXcell	Cat# BE0108; RRID: AB_10949298
InVivoMAb anti-mouse CTLA-4 (CD152) (Clone 9H10)	BioXcell	Cat# BE0131; RRID: AB_10950184
*InVivo*MAb rat IgG2a isotype control	BioXcell	Cat# BE0089; RRID: AB_1107769
anti-IL-2 monoclonal antibody (Clone JES6-1)	BioXcell	Cat# BE0043; RRID: AB_1107702
*InVivo*MAb polyclonal Syrian hamster IgG	BioXcell	Cat# BE0087; RRID: AB_1107782
Biotin anti-mouse/human CD44 Antibody (Clone IM7)	BioLegend	Cat# 103004; RRID: AB_312955
Biotin anti-mouse CD45R (B220) Monoclonal Antibody (Clone RA3-6B2)	eBioscience™	Cat# 13-0452-85; RRID: AB_466448
Biotin anti-mouse CD11b Monoclonal Antibody (Clone M1/70)	eBioscience™	Cat# 13-0112-85; RRID: AB_466360
Biotin anti-mouse CD11c Monoclonal Antibody (Clone N418)	eBioscience™	Cat# 13-0114-85; RRID: AB_466363
Biotin anti-mouse CD25 Antibody (Clone PC61)	BioLegend	Cat# 102004; RRID: AB_312853
Biotin anti-mouse CD8a Antibody (Clone 53-6.7)	BioLegend	Cat# 100704; RRID: AB_312743
Biotin anti-mouse F4/80 Antibody (Clone BM8)	BioLegend	Cat# 123106; RRID: AB_893501
Biotin anti-mouse TCR©/™ Antibody (Clone GL3)	Biolegend	Cat# 118103; RRID: AB_313827
Biotin anti-mouse Ly-6G/Ly-6C Monoclonal Antibody (Clone RB6-8C5)	eBioscience™	Cat# 13-5931-85; RRID: AB_466801
Biotin anti-mouse TER-119/Erythroid Cells Antibody (Clone TER-119)	BioLegend	Cat# 116204; RRID: AB_313705
Chemicals, peptides, and recombinant proteins		
Murine IL-2	Novoprotein	Cat# CK24
Diphtheria Toxin	Sigma-Aldrich	Cat# D0564
DNase I	Roche	Cat# 10104159001
DMEM	Gibco	Cat# c11995500BT
DTT	Merck-roche	Cat# 10708984001
CellTracker™ Red CMTPX Dye	Thermo Fischer Scientific	Cat# C34552
Collagenase IV	Sigma-Aldrich	Cat# V900893-1g
Ovalbumin (OVA)	Sigma-Aldrich	Cat# A5503-50G
1640 RPMI	Gibco	Cat# C22400500BT
FTY720	Sigma-Aldrich	Cat# SML0700
Liberase TL	Roche	Cat# 5401020001
Cell trace violet cell proliferation kit	Thermo Fischer Scientific	Cat# C34571
Percision Count Beads™	BioLegend	Cat# 424902
Fixation/Permeabilization Concentrate	Invitrogen	Cat# 2220750
eBioscience™ Fixation/Perm Diluent	Invitrogen	Cat# 2203536A
Percoll™	GE Healthcare	Cat# 17-0891-09
ACK lysing buffer	Gibco	Cat# A1049201
0.5M EDTA	Invitrogen	Cat#2085657
Fixation and Permeabilization Solution	BD Biosciences	Cat# 554722
Normal Donkey Serum	Jackson ImmunoResearch Laboratories, Inc	Cat# 017-000-121; RRID: AB_2337258
Normal Goat Serum	Jackson ImmunoResearch Laboratories, Inc	Cat# 005-000-121; RRID: AB_2336990
Normal Mouse Serum	Jackson ImmunoResearch Laboratories, Inc	Cat# 015-000-120; RRID: AB_2337194

(*Continued on next page*)

Continued

REAGENT or RESOURCE	SOURCE	IDENTIFIER
Normal Rat Serum	Jackson ImmunoResearch Laboratories, Inc	Cat# 012-000-120; RRID: AB_2337141
Normal Rabbit Serum	Jackson ImmunoResearch Laboratories, Inc	Cat# 011-000-120; RRID: AB_2337123
Ampicillin	Gold Biotechnology	Cat# A-301-100
Kanamycin	Gold Biotechnology	Cat# K-120-100
Vancomycin	Gold Biotechnology	Cat# V-200-25
Neomycin sulfate	Gold Biotechnology	Cat# N-620-100
Metronidazole	Sigma-Aldrich	Cat# M3761-25G
Streptavidin Magnetic Beads	MedChemExpress	Cat# HY-K0208
PBS	HyClone	Cat# SH30256.01
FBS	Hyclone	Cat# SH30071.03
Penicillin-Streptomycin, Liquid	Thermo Fischer Scientific	Cat# 15140122
Tirton X-100	Sangon Biotech	Cat#A600198-0500
Tissue-Tek® O.C.T. Compound	Sakura Finetek	Cat# 4583
Sucrose	Sigma-Aldrich	Cat# v900116
Bovine Serum Albumin	Sigma-Aldrich	Cat# B2064-100G
Histodenz	Sigma-Aldrich	Cat# D2158
N-Methylacetamide	Sigma-Aldrich	Cat# M26305-500G
1-Thioglycerol	Aladdin Biochemical Technology	Cat# T141418-50g
dNTP mix	Fermentas	Cat# R0192
Superscript II reverse transcriptase	Invitrogen	Cat# 18064-014
Recombinant RNase inhibitor	Clontech	Cat# 2313A
Betaine solution	Sigma-Aldrich	Cat# B0300-1VL
Magnesium chloride	Sigma-Aldrich	Cat# M8266
KAPA HiFi HotStart ReadyMix (2×)	Biosystems	Cat# KK2601
VAHTS DNA Clean Beads	Vazyme	Cat# N411-01
BCA protein assay kit	Thermo Fisher Scientific	Cat# 23227
Deposited data		
scRNA-seq and RNA-seq dataset GSE234186	This paper	GEO: GSE234186
Experimental models: Organisms/strains		
Mouse: C57BL/6	The Jackson Laboratory	JAX: 000664
Mouse: *Apc*$^{Min/+}$	The Jackson Laboratory	JAX: 002020
Mouse: *Foxp3*^{DTR}	The Jackson Laboratory	JAX:016958
Mouse: *Ubi-GFP*	The Jackson Laboratory	JAX:006148
Mouse: *Villin-cre*	The Jackson Laboratory	JAX:018963
Mouse: *Apc*$^{LoxP/+}$	The Jackson Laboratory	JAX:009045
Mouse: *OVA*$_{257-264}$*-specific T cell transgenic OT-I*	The Jackson Laboratory	JAX:003831
Mouse: *OVA*$_{323–339}$*-specific T cell -receptor transgenic OT-II*	The Jackson Laboratory	JAX:004194
Mouse: *Tcra KO*	The Jackson Laboratory	JAX:002116
Mouse: *Foxp3-cre*	The Jackson Laboratory	JAX:016958
Mouse: *Nr4a1*^{EGFP}	The Jackson Laboratory	JAX: 016617
Mouse: *Ccr4*$^{-/-}$	Gempharmatech	T052841
Mouse: *Ccr4*$^{fl/fl}$	Gempharmatech	T052007
Mouse: *Ubi-tdTomato*	From Dr. Ronald N. Germain, NIAID, NIH	N/A
Mouse: *Ccl22-tdTomato*	From Dr. Qi Hai, Tsinghua University	N/A

(*Continued on next page*)

Continued

REAGENT or RESOURCE	SOURCE	IDENTIFIER
Software and algorithms		
Prism 8	Graphpad	https://www.graphpad.com/
FlowJo version 10.5.3	Treestar	https://www.flowjo.com/
ImageJ	Freeware/NIH	https://imagej.nih.gov/ij/
Imaris 10.0	Bitplane	https://imaris.oxinst.com/
R 4.3.2	N/A	https://www.r-project.org/
Seurat 4.3.0	https://www.nature.com/articles/nbt.4096	https://satijalab.org/seurat
Harmony	Korsunsky et al., 2018	https://github.com/pardeike/Harmony
ImageScope	Leica Biosystems	https://www.leicabiosystems.com/
CellProfiler (v3.1.9)		https://cellprofiler.org/
Leica LAS X Suite software	Leica	N/A

RESOURCE AVAILABILITY

Lead contact

Further information and requests for resources and reagents should be directed to and will be fulfilled by the lead contact, Kairui Mao (maok@xmu.edu.cn).

Materials availability

This study did not generate new unique reagents.

Data and code availability

- Single-cell RNA-seq data and RNA-seq data have been deposited at GEO and are publicly available as of the date of publication. Accession numbers are listed in the key resources table.
- This paper does not report original code.
- Any additional information required to reanalyze the data reported in this paper is available from the lead contact upon request.

EXPERIMENTAL MODEL AND STUDY PARTICIPANT DETAILS

Animals

C57BL/6 (Jax stock, 000664), *Apc*$^{Min/+}$ (Jax stock, 002020), *Foxp3*^{DTR} (Jax stock, 016958), *Foxp3-cre* (Jax stock, 016959), *Tcra*$^{-/-}$ (Jax stock, 002116), *Ubi-GFP* (Jax stock, 007076), *Villin-cre* (Jax stock, 004586), *Apc*$^{fl/fl}$ (Jax stock, 029275), *Tcra*$^{-/-}$ (Jax stock, 002116), *Nr4a1*^{EGFP} (Jax stock, 016617), $OVA_{323–339}$-specific T cell -receptor transgenic OT-II (Jax stock, 004194) and $OVA_{257-264}$-specific T cell transgenic OT-I (Jax stock, 003831) mice were originally from the Jackson Laboratories. *Ccr4*$^{-/-}$ mice (Strain No. T052841) and *Ccr4*$^{fl/fl}$ mice (Strain No. T052007) were purchased from GemPharmatech (Nanjing, China). *Ccl22*^{tdTomato}[56] and *Ubi-tdTomato*[76] mice as previously reported were kindly provided by Dr. Hai Qi (Tsinghua University) and Dr. Ronald N. Germain (National Institute of Allergy and Infectious Diseases, National Institutes of Health), respectively. All mice were maintained under specific pathogen-free condition at the Laboratory Animal Center, Xiamen University. All animal experiments were approved by the Institutional Animal Care and Use Committee and were in strict accordance with good veterinary practice as defined by the Xiamen University Laboratory Animal Center.

Human specimens

Treatment-naïve patients pathologically diagnosed with colorectal cancer and colorectal polyp were included in this study (Table S3). Specimens were harvested after Radical Resection of CRC and Endoscopic Mucosal Resection respectively at Zhongshan Hospital, Xiamen University (Xiamen, Fujian, China) in accordance with the guidelines of the institutional review board. This study complies with all relevant ethical regulations and was approved by the Ethics Committee of Zhongshan Hospital Xiamen University. All participants signed an informed consent form before enrolment.

Cell lines and primary cell culture

The mouse lung adenocarcinoma cell line (KP cell) was kindly provided by Dr. Hongbin Ji (Center for Excellence in Molecular Cell Science, University of Chinese Academy of Sciences) as previously described.[77] KP cells were cultured in RPMI1640 with 10% fetal bovine serum, 50 mM 2-mercaptoethanol, 100 U/mL Penicillin, 100 μg/mL Streptomycin and 292 μg/mL L-Glutamine.

METHOD DETAILS

Immunofluorescence staining and confocal imaging

Immunofluorescence staining and confocal imaging were performed as previously described.[78] Briefly, the ileum or colon tissues with or without tumors were excised and prepared using the Swiss roll technique, fixed with BD Cytoperm/Cytofix (BD Bioscience, Cat#: 554722) solution (diluted with PBS at 1:2) overnight at 4°C, followed by dehydrated in 30% sucrose for 12-16 hours before embedding in OCT compound (Sakura Finetek, Cat#: 4583). 16-μm sections were prepared using a CM1905 cryostat (Leica) and adhered to positively charged slides (Premiere). Frozen sections were rehydrated with phosphate-buffered saline (PBS), then blocked with PBS containing 1% normal mouse serum, 1% bovine serum albumin, and 0.3% Triton X-100, followed by sequential staining with unconjugated primary antibodies overnight at 4°C, fluorescent conjugated secondary antibodies for 2-3 hours at room temperature and directly conjugated antibodies for 24 hours at room temperature in a dark humidified chamber. Sections were washed with PBS for 3-5 times (5 min per wash) between each staining steps. All antibodies were diluted in blocking buffer. The following antibodies were used for staining: anti-B220 (RA3-6B2, eBioscience), anti-CCL21 (polyclonal goat IgG, R&D Systems), anti-CD11c (N418, BioLegend), anti-CD3 (17A2, BioLegend), anti-CD31 (MEC13.3, BioLegend), anti-CD4 (RM4-5, BD Biosciences), anti-CD8 (53-6.7, BioLegend), anti-EpCAM (G8.8, BioLegend), anti-F4/80 (BM8, eBioscience), anti-Foxp3 (AFKJS-9, eBioscience), anti-GFP (BioLegend), anti-Ki67 (B56, BD Biosciences), anti-Lyve1 (ALY7, eBioscience), anti-MHC-II (M5/114.15.2, BioLegend), anti-RFP (polyclonal rabbit IgG, Rockland), anti-OX-40 (EPR22229-5, Abcam) and anti-PD-1 (RMP1-30, BioLegend). After staining, slides were mounted with Fluormount G (Southern Biotech, Cat#: 0100-01) and images were acquired on a Leica TCS SP8 or Leica STELLARIS 8 STED confocal microscope. Images were analyzed with Imaris software (Bitplane).

Human tissue specimens were provided by Zhongshan Hospital, Xiamen University under an approved Institutional Review Board protocol. The specimens were collected within 30 min after the tumor resection and incubated in BD Cytoperm/Cytofix solution (BD Bioscience, Cat#: 554722) overnight followed by dehydration in 30% sucrose before embedding in OCT compound (Sakura Finetek, Cat#: 4583). 16-μm sections were prepared on a CM1905 cryostat (Leica) and adhered to positively charged slides (Premiere). Frozen sections were rehydrated with phosphate-buffered saline (PBS), then blocked with PBS containing 2% normal goat serum, 1% bovine serum albumin, and 0.3% Triton X-100, followed by sequential staining with unconjugated primary antibodies overnight at 4°C, fluorescent conjugated secondary antibodies for 2-3 hours at room temperature and directly conjugated antibodies for 24 hours at room temperature in a dark humidified chamber. Sections were washed with PBS for 3-5 times (5 min per wash) between each staining steps. All antibodies were diluted in blocking buffer. The following antibodies were used for staining: anti-Lyve1 (polyclonal rabbit IgG, Abcam), anti-Podoplanin (NC-08, Biolegend), anti-CD3 (UCHT1; BioLegend), anti-CD4 (RPA-T4, BD Biosciences), anti-Foxp3 (236A/E7, Invitrogen), anti-Ki67 (B56, BD Biosciences). After staining, slides were mounted with Fluormount G (Southern Biotech, Cat#: 0100-01) and images were acquired on a Leica TCS SP8 or Leica STELLARIS 8 STED confocal microscope. Images were analyzed with Imaris software (Bitplane).

3D imaging of mouse tumor

Clearing-enhanced 3D imaging (Ce3D) of mouse colon tumors were performed as previously described.[48] Briefly, colon tumors from 16-week-old male *Apc*$^{Min/+}$ mice or *Apc*$^{Min/+}$*Ccl22*^{tdTomato} mice were harvested and fixed with BD Cytoperm/Cytofix solution (diluted 1:2 in PBS) at 4°C overnight. Following 3 times washes in PBS (1 hour per wash), tumors were incubated in 1 mL blocking buffer (PBS with 1% normal mouse serum, 1% normal goat serum, 1% bovine serum albumin and 0.6% Triton X-100) at 4°C for 24 hours with shaking (60 rpm). For immunostaining, tumors were incubated sequentially with anti-RFP (Rockland Immunochemicals, Cat#: 600-401-379) primary antibody for 3 days, goat-anti-rabbit secondary antibodies (Life Technologies, Cat#: 2134003) for 2 days, directly conjugated antibodies for 3 days diluted in blocking buffer and Hoechst 33342 (Thermo Fisher Scientific, Cat#: H21492) for 4-6 hours. All the staining steps were performed at 4°C with shaking (60 rpm) and followed by 3 times washes in PBS (8 hours per wash) at room temperature with shaking (100 rpm). The following antibodies were used for staining: anti-CD4 (RM4-5, BD Biosciences), anti-Foxp3 (AFKJS-9, eBioscience), anti-Lyve1 (ALY7, eBioscience). Stained tumors were incubated in freshly prepared Ce3D tissue clearing solution (40% (v/v) N-methylacetamide (Sigma-Aldrich, Cat#: M26305), 80% (w/v) Histodenz (Sigma-Aldrich, Cat#: D2158), 0.1% (v/v) Triton X-100, and 0.5% (v/v) 1-thioglycerol (Sigma-Aldrich, Cat#: M1753)) at 4°C on a rotor overnight. After clearing, tumors were embedded in Ce3D medium within a vacuum grease or silicone gel spacer on a microscope slide tightly covered with a No. 1.5 cover glass. Images were acquired on a Leica TCS SP8 confocal microscope, then analyzed with Imaris software (Bitplane) and Adobe Premiere Pro.

Preparation of cell suspensions, antibody staining and flow cytometry

For isolation of lymphocytes from colonic lamina propria or tumors, tissue segments were treated with RPMI 1640 (Gibco, Cat#: C22400500BT) containing 0.5 mM EDTA (Sigma-Aldrich, Cat#: 2085657) and 0.145 mg/mL dithiothreitol (Merck-roche, Cat# 10708984001) for 30 min at 37°C with constant stirring to remove epithelial cells. Tissues were minced and further digested with 0.5 mg/mL collagenase IV (Sigma-Aldrich, Cat#: V900893-1g) and 100 μg/mL DNase I (Roche, Cat#: 10104159001) in RPMI 1640 containing 10% FBS with continuous stirring at 37°C for 30 min. Digested tissues were passed through a 70- and 40-μm cell strainer and lymphocytes were enriched using Percoll (GE Healthcare, Cat#: 17-0891-09) gradient centrifugation. The cell suspensions were stained with the fixable viability violet dyes Zombie Red or Fixable Viability Dye eFluor™ 780 (Invitrogen) for 30 min at 4°C, followed by blocking of Fc receptors with anti-CD16/32 (2.4G2, BD Biosciences) for 15 min at 4°C. Cell surface proteins were stained for 30 min at

4°C with the following antibodies: anti-CD45 (30-F11), anti-CD3 (17A2), anti-CD4 (GK1.5), anti-TCRβ (H57-597), anti-PD-1 (29F.1A12), anti-CTLA-4 (UC10-4B9), anti-CD366/TIM-3 (RMT3-23), all from BioLegend, and anti-CD25 (PC61.5), anti-CD45R/B220 (RA-6B2), anti-ICOS(7E.17G9), anti-OX40 (OX-86) from eBioscience. Nuclear proteins were stained overnight at 4°C after permeabilization and fixation (Mouse regulatory T cell staining Kit, eBioscience, Cat#:88-8115-40) using anti-Foxp3 (FJK-16s) from eBioscience.

For isolation of myeloid cells (DCs, monocytes and macrophages) from tumors, tissue segments were minced and further digested with 0.5 mg/mL collagenase IV (Sigma-Aldrich, Cat#: V900893-1g) and 100 μg/mL DNase I (Roche, Cat#: 10104159001) in RPMI 1640 containing 10% FBS with continuous stirring at 37°C for 30 min. Digested tissues were passed through a 100-μm cell strainer and myeloid cells were enriched with Percoll (GE Healthcare, Cat#: 17-0891-09) gradient centrifugation. The cell suspensions were stained with the fixable viability violet dyes Zombie Red or Fixable Viability Dye eFluor™ 780 (Invitrogen) for 30 min at 4°C, followed by blocking of Fc receptors with anti-CD16/32 (2.4G2, BD Biosciences) for 15 min at 4°C. Cell surface proteins were stained for 30 min at 4°C with the following antibodies: anti-CD45 (30-F11), anti-CD64 (X54-5/7.1), anti-Ly-6C (HK1.4), anti-I-A/I-E (M5/114.15.2), anti-CD80 (16-10A1), anti-CD86 (GL-1), anti-CCR7 (4B12), anti-CTLA-4 (UC10-4B9), all from BioLegend, and anti-CD11c (HL3) , anti-CD11b(M1/70) from eBioscience.

For analysis of migratory and resident dendritic cells in tumor draining lymph nodes, mesenteric lymph nodes were digested with 0.5 mg/mL collagenase IV and 100 μg/mL DNase I in RPMI 1640 containing 10% FBS at 37°C for 30min, and passed through 70-and 40-μm cell strainers. The cell suspension was stained with the fixable viability violet dyes Zombie Red or Fixable Viability Dye eFluor™ 780 (Invitrogen) for 30 min at 4°C, followed by blocking of Fc receptors with anti-CD16/32 (2.4G2, BD Biosciences) for 15 min at 4°C. Cells were washed and incubated with a mixture of monoclonal antibodies containing anti-CD45 (30-F11), anti-CD3 (17A2), anti-I-A/I-E (M5/114.15.2), all from BioLegend, and anti-CD11c (HL3), anti-CD45R/B220 (RA-6B2) from eBioscience. The cell counts were normalized to a predetermined number of counting beads (BioLegend, Cat#: 424902). Cells were analyzed on Beckman Cytoflex LX, LSRFortessa or LSRFortessa X-20 flow cytometers (BD Biosciences) and data were analyzed with FlowJo software version 10.5.3.

Single cell segmentation and quantification

Image files generated in LAS X software were converted into ''.ims'' files in Imaris software (Bitplane) and subjected to a 1 pixel Gaussian filter to reduce noise. Single cell segmentation of multiplex immunofluorescence images was performed by CellProfiler (Version 3.1.9).[79] In the CellProfiler setting, we first identified nuclei using Hoechst channel, then defined cell borders by expanding 3 pixels and generated cell masks from original images. Single cell fluorescence for each protein was quantified as mean intensity by *skimage.measure.regionprops* function (Python package, Version 0.15.0). Based on the cell lineage marker expression, we annotated cells as Tregs ($CD4^+$ $Foxp3^+$), macrophages ($F4/80^+$) and DCs ($CD11c^+$). Tumor margin was drawn by ImageScope (Leica Biosystems) based on the staining of Ki67. The distance between immune cells and tumor margin was measured by the nearest distance of cell center to points on the tumor edge. For each cell, we set the sign of distance as positive if the cell was inside the tumor and negative if the cell was outside the tumor.

Quantitative image and spatial analysis

To quantify the distance of Tregs to blood and lymphatic vessels in colon tumors from $Apc^{Min/+}$ mice, Foxp3, Lyve1, CD31 channels were reconstructed by the Surface function of the Imaris software. Tregs were defined as $Foxp3^+CD4^+$ cells, lymphatic and blood vessels was defined as $Lyve1^+CD31^{int}$ and $Lyve1^-CD31^+$, respectively. For each Treg, the minimum distance to blood and lymphatic vessels was measured by the shortest distance to surfaces (set to $Lyve1^+CD31^{int}$ and $Lyve1^-CD31^+$ channel, respectively) in Imaris software. Individual Treg statistics, including the distance to blood and lymphatic vessels were exported as ''.csv'' files and imported into the Prism for further analysis.

To quantify the distance of Tregs to lymphatic vessels in human tumor, Foxp3 and Podoplanin channels were reconstructed by the Surface function of the Imaris software. $Foxp3^+CD4^+$ cells and $Podoplanin^+$ were defined as Tregs and lymphatic vessels, respectively. For each Treg, the minimum distance to lymphatic vessels was measured by the shortest distance to surfaces (set to $Podoplanin^+$ channel) in Imaris software. Individual Treg statistics, including the distance to lymphatic vessels were exported as ''.csv'' files and imported into the Prism for further analysis.

To quantify the association of Tregs and DC subsets in colon tumors from $Apc^{Min/+}$ $Ccl22^{tdTomato}$ mice, Foxp3, $CCL22^{tdTomato}$, CD103, CD11b and Lyve-1 channels were reconstructed by the Surface function of the Imaris software. $Foxp3^+CD4^+$ was defined as Tregs, $MHC\text{-}II^+CCL22^{tdTomato+}$ was defined as mregDCs, $MHC\text{-}II^+CCL22^{tdTomato-}CD103^+$ was defined as cDC1s, $MHC\text{-}II^+CCL22^{tdTomato-}CD11b^+F4/80^-$ was defined as cDC2s, and $Lyve1^+$ was defined as lymphatic vessels respectively. For each Treg and DCs, the minimum distance to DC subsets and the minimum distance to lymphatic vessels were measured by the shortest distance to surfaces in Imaris software. Individual Treg and DC statistics, including the distance information were exported as ''.csv'' files and imported into the R and Prism for further analysis and visualization.

To quantify the association of Tregs and mregDCs and PD-1 intensity on Tregs in colon tumors from $Apc^{Min/+}$ $Ccl22^{tdTomato}$ mice treated with control or anti-$I\text{-}A^b$ antibody. Foxp3, $CCL22^{tdTomato}$ and Lyve-1 channels were reconstructed by the Surface function of the Imaris software. $Foxp3^+CD4^+$ was defined as Tregs, $MHC\text{-}II^+CCL22^{tdTomato+}$ was defined as mregDCs, and $Lyve1^+$ was defined as lymphatic vessels respectively. For each Treg and mregDC, the minimum distance to mregDC or the minimum distance to lymphatics were measured by the shortest distance to surfaces in Imaris software. Individual Treg and mregDC statistics, including the

distance and fluorescence intensity values of PD-1 channel were exported as ".csv" files and imported into the R and Prism for further analysis and visualization.

To quantify the association of Tregs and mregDCs and PD-1 intensity on Tregs in colon tumors from irradiated $Apc^{Min/+}$mice transferred with GFP$^+$ $Ccr4^{-/-}$ bone marrow (BM) cells mixed with $Ccl22^{tdTomato}$ BM cells at 1:1 ratio. Foxp3, CCL22^{tdTomato} and Lyve-1 channels were reconstructed by the Surface function of the Imaris software. Foxp3$^+$CD4$^+$ was defined as Tregs, Foxp3$^+$CD4$^+$GFP$^+$ was defined as CCR4$^{-/-}$ Tregs, Foxp3$^+$CD4$^+$GFP$^-$ was defined as WT Tregs, MHC-II$^+$CCL22$^{tdTomato+}$ was defined as mregDCs, and Lyve1$^+$ was defined as lymphatic vessels respectively. For each Treg, the minimum distance to mregDC was measured by the shortest distance to surfaces in Imaris software. Individual Treg statistics, including the distance and fluorescence intensity values of PD-1 channel were exported as ".csv" files and imported into the R and Prism for further analysis and visualization.

To explore the correlation between the distance to mregDCs and Treg activation markers (PD1 and OX-40) expression on Tregs. Foxp3, CCL22-tdTomato signals were reconstructed through the surface function of the Imaris software. Foxp3$^+$CD4$^+$ was defined as Tregs, CCL22-tdTomato$^+$ CD11c$^+$ was defined as mregDCs. For each Treg, the distance to mregDCs was measured by the minimum distance to surfaces (set to CCL22-tdTomato channel) in Imaris software. And the activation markers expression in Tregs was quantified as max intensity. Individual Treg statistics, including distance to mregDCs and fluorescence intensity values of PD-1 or OX-40 channel were exported as ".csv" files and imported into the R statistical environment for further analysis. The further analysis process was as follows: first, the fluorescence value of activated molecules (PD-1 and OX-40) of each tumor was normalized and then scaled to the (0, 255) interval to reduce the influence of individual differences on the fluorescence value. Then, calculated the median of the fluorescence intensity and set the part greater than the median as PD1/OX-40^{hi}. Finally, the proportions of these Tregs were calculated with a boundary of 70 μm for statistical analysis.

Antibiotics, antibody and diphtheria toxin (DTX) treatment

4-week-old male $Apc^{Min/+}$ mice were provided with ampicillin (1 g/L) (Gold Biotechnology, Cat#: A-301-100), kanamycin (5 g/L) (Gold Biotechnology, Cat#: K-120-100), vancomycin (500 mg/L) (Gold Biotechnology, Cat#: V-200-25), neomycin sulfate (1 g/L) (Gold Biotechnology, Cat#: N-620-100) and metronidazole (1 g/L) (Sigma, Cat#: M3761-25G) in drinking water for 12 weeks. After treatment, colon tumors were harvested for imaging.

16-week-old male $Apc^{Min/+}$ mice were treated intraperitoneally with 200 μg of anti-CTLA-4 (Clone 9H10, BioXcell, Cat#: BE0131) antibodies or control antibodies (Rat IgG2a, BioXcell, Cat#: BE0089; Syrian hamster IgG, BioXcell, Cat#: BE0087) for three times on every other day.

16-week-old male $Apc^{Min/+}$ mice were intra-tumorally injected with 50μg of anti-MHC-II (Clone M5/114, BioXcell, Cat#: BE0146) antibodies or control antibodies (Rat IgG2a, BioXcell, Cat#: BE0108; Syrian hamster IgG, BioXcell, Cat#: BE0087). Tumors were harvested 48 hours post treatment.

For short term Treg depletion, 16-week-old $Apc^{Min/+}Foxp3^{DTR}$ mice were intraperitoneally injected with 250 ng of DTX (Sigma-Aldrich, Cat#: D0564) diluted in 100 μL sterile PBS on every other day for three times. For long term Treg depletion, two rounds (3 times on every other day for each round) of DTX at an interval of 3 weeks were administered into 6-week-old $Apc^{Min/+}Foxp3^{DTR}$ mice.

Bulk Treg cell RNA sequencing

Tregs (CD45$^+$CD3$^+$CD4$^+$CD25$^+$GFP$^+$) were sort-purified from colon tissues or tumors from $Foxp3^{DTR}$ and $Apc^{Min/+}Foxp3^{DTR}$ mice, respectively. Cells were collected into tubes with lysis buffer and ribonuclease inhibitor. Full-length RNA-seq libraries were prepared following a modified SMART-Seq2 protocol.[80] Briefly, oligo dT primers were introduced to the reverse transcription reaction for first strand cDNA synthesis, followed by PCR amplification and enrichment of the DNA library with magnetic beads to clean up the products. Sequencing libraries were generated using TruePrep® DNA Library Prep Kit V2 for Illumina® (Vazyme Biotech, Cat#: TD502) following manufacturer's instructions and index codes were added to attribute sequences to each sample. After the library preparation was completed, the library concentration was quantified using real-time PCR and the library quality was evaluated on the Agilent Bioanalyzer 2100 system (Agilent Technologies). The clustering of the index-coded samples was performed on a cBot Cluster Generation System using TruSeq PE Cluster Kit v3-cBot-HS (Illumina) according to the manufacturer's instructions. After cluster generation, the library preparations were sequenced on an Illumina Novaseq 6000 platform and 150 bp paired-end reads were generated. The image data measured by the high-throughput sequencer were converted into sequence reads by CASAVA base recognition. Raw reads of ".fastq" format were firstly processed through in-house perl scripts. In this step, clean reads were obtained by removing reads containing adapter, reads containing N base and low-quality reads from raw data. Index of the reference genome (mm10) was built using Hisat2 (v2.0.5) and paired-end clean reads were aligned to the reference genome using Hisat2. Gene counts were derived from the number of uniquely aligned unambiguous reads by featureCount (v1.5.0-p3). And then FPKM of each gene was calculated based on the length of the gene and reads count mapped to this gene. Differential expression analysis of two conditions/groups (two biological replicates per condition) was performed using the DESeq2 R package (1.20.0). padj<=0.05 and |log2(fold-change)| >= 1 were set as the threshold for significantly differential expression. The differentially expressed genes were used for further analysis.

TCR sequencing and analysis

Tregs (CD45$^+$CD3$^+$CD4$^+$CD25$^+$) were sort-purified from colon tissues or tumors from WT and $Apc^{Min/+}$ mice, respectively. Cells were lysed with lysis buffer and ribonuclease inhibitor. Total RNA was extracted and reverse transcribed into cDNA using the Smart-Seq2

protocol.[80] After the first-strand reaction, the cDNA was amplified for 13 cycles according to the Smart-Seq2 protocol. In order to remove contamination from primers from the previous step, VAHTS DNA Clean Beads (Vazyme, N411) were used to purify the products after each round of PCR. A two-round nested PCR was then performed using primers specific for TCRα and TCRβ. For the first round of PCR, 4.4 μL of reverse-transcribed product was used as a template, and the TCRα primer (5'-ctggttgctccaggcaatgg-3') and TCRβ primer (5'-tgtaggcctgagggtccgt-3') were used to specifically amplify TCRα and TCRβ. Subsequently, all product was used in the second round of PCR and the primers (TCRα: 5'- agtcaaagtcggtgaacaggca-3', TCRβ: 5'-ggccaagcacacgagggta-3') were used. The amplicons were purified using VAHTS DNA Clean Beads and subjected to paired-end sequencing (2 × 150 bp) on an Illumina platform (NovaSeq X Plus-PE150) according to standard protocols. The sequencing data was obtained after filtering low-quality sequences using a standard procedure. Alignment was performed using the RNA-seq pipeline in MIXCR v4.6.0[2].[81]

The CDR3 ratio was calculated based on read counts associated with each CDR3. The "Top10 clones" refer to the top ten clones ranked by CDR3 ratio, while "high frequency clones" encompass the first 100 clones, with subsequent clones categorized as "low frequency clones". Custom R scripts and ggplot2 package (version 3.5.0) were used for further analysis and visualization.

Isolation of CD45$^+$ immune cells from colon tissues or tumors for scRNAseq

Single cell suspensions collected from colon tumor from *Apc$^{Min/+}$* mice and colon tissues from WT mice were stained with fixable viability violet dye Zombie Red and anti-CD45 (30-F11) (BioLegend) and sorted by BD FACS Aria Fusion Cell Sorter. Cells were stained with trypan blue to check viability and counted using light microscopy, then loaded onto a 10x Chromium microfluidics system according to the manufacturer's guidelines. Prepared single-cell suspension was partitioned into GEMs (Gel Beads in Emulsions) in the automated Chromium Controller, and then mRNAs were reverse transcribed into cDNAs. ScRNA-seq libraries were prepared using the Chromium Single Cell 3′ Reagent Kits v2 (10x Genomics) according to the manufacturer's instructions. All the subsequent steps were performed following the standard manufacturer's protocols. Purified libraries were sequenced by the DNBSEQ, followed by de-multiplexing and mapping to the mouse genome using CellRanger (10x Genomics, Version 2.1.1).

Single cell RNA sequencing analysis

The sequencing reads were examined by quality metrics, and transcripts were mapped to a reference mouse genome (mm10) and assigned to individual cells of origin according to the cell-specific barcodes, using the Cell Ranger pipeline (10x Genomics). Transcriptomes with more than or equal to 200 total features, less than or equal to 4000 total features (to filter out doublets), less than 15% of total features derived from mitochondrial genes were retained. A total of 23, 922 cells were obtained for downstream analyses, of which 14, 445 cells were from tumor and the remaining 9, 477 cells were from colon tissues.

To integrate cells into a shared space from different samples for unsupervised clustering, we used the harmony algorithm to integrate two datasets.[82] In general, Harmony was run with the *RunHarmony* function in Seurat, and using the Harmony embeddings instead of PCA in downstream analysis. A nearest neighbor graph and UMAP were created with the functions *FindNeighbors* and *runUMAP* from the Seurat package. The difference from the standard Seurat process is using the corrected Harmony embeddings rather than PCs, set reduction = "harmony" when performing *RunUMAP* and *FindNeighbors* function.

The first round of clustering identified eight major cell types including B cell, neutrophil, monocyte, T/ILC, macrophage, DC, mast cell and an undefined cluster. To identify clusters within T/ILC, we used the subset function to extract all T and ILCs and then performed a second round of clustering. The procedure of the second round of clustering was the same as first round, starting from unfiltered expression matrix, including finding HVGs, calculating PCA matrix and performing integration analysis by Harmony. For dimension reduction, we calculated UMAP using batch-corrected shared space output by Harmony. The second round of clustering also identified seven major cell types including CD8$^+$ T cells (*Cd8a*), Tregs (*Cd4* and *Foxp3*), CD4$^+$ conventional T cells (*Cd4* without *Foxp3*), DN T cells (*Cd3e* without *Cd4* and *Cd8a*), NK cells (*Ncr1*), ILCs (*Id2* and *Gata3* without *Cd3e*) and a mixed population of various cells defined as Others. The same operation was performed on DC population and identified four cell clusters including cDC1 (*Itgae*), cDC2 (*Itgam*), mregDC (*Ccl22*) and pDC (*Siglech*).

For gene scoring analysis, we calculated gene signatures in each cell using Seurat's *AddModuleScore* function. The myeloid-derived suppressor cells (MDSC) signatures were a selection of 10 genes (*Ly6c*, *Ly6g*, *Itgam*, *Arg2*, *Il1b*, *Wfdc17*, *Ifitm1*, *Junb*, *Csf3r* and *Cxcr2*) as reported previously.[83] The Treg activation signatures were a selection of 17 genes (*Foxp3*, *Il2ra*, *Icos*, *Tgfb1*, *Areg*, *Il10*, *Ctla4*, *Tnfrsf4*, *Tnfrsf9*, *Ccr8*, *Tnfrsf18*, *Il1r2*, *Cxcr6*, *Lag3*, *Tigit*, *Pdcd1* and *Klrg1*) as reported previously.[21] After calculated the signatures score, we set the median value to separate Treg cells to activated Treg and quiescent Treg for further comparative analysis. All heat maps were generated using pheatmap (Version 1.0.12).

Gene ontology and gene sets enrichment analysis

Gene Ontology functional enrichment (overrepresentation) of DEGs at $P < 0.05$ was analyzed using R package clusterProfiler (Version 4.2.2). Gene Set Enrichment Analysis (GSEA) also conducted using R package clusterProfiler (Version 4.2.2), normalized enrichment scores were acquired using gene set permutations 1000 times, and a cutoff P-value of 0.05 was used to filter the significant enrichment results.

Cell-cell interaction analysis

To identify potential interactions between and within T cells and DC subpopulations, we used CellPhoneDB 3.0[84] with parameters threshold = 0.1 and iterations = 1000, which contains a curated repository of ligand–receptor interactions and a statistical framework

for inferring lineage-specific interactions. It is worth noting that CellPhoneDB is a human interaction database, so it is necessary to convert human-mouse homologous genes by R package biomaRt (Version 2.50.3) first. Custom R scripts and circlize package (Version 0.4.15) were used for analyses and to draw the interaction diagrams.

KP cell line and mouse model

KP cells were cultured in RPMI1640 with 10% fetal bovine serum, 50mM 2-mercaptoethanol, 100 U/mL Penicillin, 100 mg/mL Streptomycin and 292 μg/mL L-Glutamine. Eight-week-old male *Ccl22*^{tdTomato} mice were injected intravenously with 5×10^5 KP cells and lungs were harvested for analysis on day 27 post transfer.

FITC-OVA preparation and *in situ* injection

FITC-conjugated OVA was prepared according to the manufacturer's instructions. In brief, 20 μg FITC (Sigma-Aldrich, Cat#:27072-45-3) was dissolved in 10 mL of carbonate buffer (220 mM, pH 9.5) containing 100 mg OVA (Sigma-Aldrich, Cat#: A5503-50G). The mixture was gently stirred in the dark at 4°C for 18 h. Unbound FITC were removed by dialysis (MWCO 10000). FITC-OVA protein concentration was measured by BCA protein assay kit (Thermo Fisher Scientific, Cat#: 23227).

For *in situ* injection of FITC-OVA to simulate tumor antigen, animals were anesthetized with 1% pentobarbital sodium and colon tissues was exposed. 15 μg FITC-OVA plus 20 ng LPS in 5 μL PBS was injected into the colonic lamina propria or the tumors of WT and *Apc*$^{Min/+}$ mice, respectively. 24 hours after injection, FITC$^+$ migratory and resident dendritic cells in mesenteric lymph nodes were measured by flow cytometry.

Mixed bone marrow chimeras

To ablate bone marrow cells, 6-week-old male *Apc*$^{Min/+}$ recipient mice were irradiated with a lethal dose of 9.5 Gray in the RS-2000 irradiator (Rad Source). Donor bone marrow was extracted from the femurs and tibias by PBS perfusion with a 21-gauge needle. Red blood cells were lysed by ACK lysing buffer (Gibco, Cat#: A1049201) and the resulting cell suspensions were filtered through a 40 μm cell-strainer prior to intravenous injection. Donor bone marrow cells were extracted from *Ccl22*^{tdTomato}, *Ubi-GFP*, *Ubi-tdTomato* and *Ccr4*$^{-/-}$ *Ubi-GFP* mice, mixed at a ratio of 1:1 (5×10^6 cells in total) and injected intravenously into irradiated recipients 6-8 hours post irradiation. Colon tumors from recipients were harvested 12 weeks after reconstitution.

T cell isolation and adoptive transfers

For *in vivo* expansion of Treg cells, *Ubi-GFP*, *Ubi-tdTomato* and *Ccr4*$^{-/-}$ *Ubi-GFP* mice were injected intraperitoneally with IL-2/IL-2-antibody complexes for three consecutive days as previously described.[85] IL-2/IL-2-antibody complexes were made by mixing 1 μg recombinant mouse IL-2 (Novoprotein, Cat#: CK24) with 5 μg anti-IL-2 monoclonal antibody (clone JES6-1, BioXcell) followed by incubation at 37°C for 30 min. Peripheral lymph nodes and spleen were homogenized in cold PBS supplemented with 1% BSA and 2mM EDTA. Cell suspensions were subsequently filtered through a 40 μm cell strainer. CD4$^+$ T cells were enriched by streptavidin magnetic bead-based negative selection. The cocktail of biotin-conjugated antibodies was mixed with anti-CD8, anti-CD11b, anti-CD11c, anti-B220, anti-Ly-6G/Ly-6C, anti-F4/80, anti-Ter119 and anti-TCRγ/δ. CD4$^+$CD25$^+$ Treg cells were purified with BD Aria III sorter. Donor Treg from *Ubi-GFP*, *Ubi-tdTomato* and *Ccr4*$^{-/-}$ *Ubi-GFP* mice were mixed at a ratio of 1:1 (5×10^6 cells in total) and transferred to 16-week-old male *Apc*$^{Min/+}$ recipient mice by intravenous injection. Three days after Treg cell transfer, tumor and mesenteric lymph nodes were harvested and Treg cells were examined by flow cytometry.

OT-I and OT-II T cells were isolated from peripheral lymph nodes and spleen of OT-I *Ubi-GFP* or OT-II *Ubi-GFP* mice by streptavidin magnetic bead-based negative selection. Purified cells were labeled with 5 μM CellTrace Violet (Thermo Fisher Scientific, Cat#: C34557) for 20 min at 37°C. Unbound dye was removed by washing cells twice with PBS supplemented with 1% BSA. 1×10^6 T cells were intravenously transferred into WT and *Apc*$^{Min/+}$ recipient mice injected with OVA/LPS into colon lamina propria or tumors. 24 hours post transfer, recipient mice were administered 150 μg of FTY720 (Sigma-Aldrich, Cat#: SML0700) daily by intraperitoneal injection for 4 consecutive days to trap transferred cells in lymphoid tissues. 5 days after T cell adoptive transfer, proliferation of OT-I and OT-II cells in mesenteric lymph nodes was examined by flow cytometry.

Spatial transcriptomic data analysis

Spatial transcriptomic data were downloaded from Alberto et al.[69] The *SpatialDimPlot* and *SpatialFeaturePlot* functions in R package Seurat (version 4.3.0) were utilized for visualization.[86] We performed gene set enrichment analysis using the ssGSEA algorithm in R package GSVA[54] to calculate enrichment scores for each cell type gene signatures (The signature genes for each cell type were listed in Table S2). Then quiescent Treg was determined by all Treg minus activated Treg. For each cell type signature, the spots with enrichment scores in the top 5% were displayed and utilized in downstream analysis. To quantify the distance between mregDC and other cell types, the distances to the three nearest spots were averaged. The Wilcox test was applied to determine the statistical significance of differences between groups.

TCGA data analysis

The TCGA colon adenocarcinoma (COAD), breast cancer (BRCA), lung adenocarcinoma (LUAD) and melanoma (SKCM) data were used to test the correlation of selected genes and cell populations. The gene expression data were downloaded from UCSC Xena (http://xena.ucsc.edu/). For single gene correlation analysis, selected gene expression (RNA-seq transcript per million mapped reads

(TPM)) correlation was performed in R using two-tailed Pearson correlation coefficients analysis. For multiple signatures of specific cell type correlation analysis, Treg and mregDC gene signature expression scores were computed based on signatures (*FOXP3*, *CTLA4*, *CCR8* and *TNFRSF9* for Treg; *CCL22*, *CCR7*, *FSCN1* and *CD1C* for mregDC) using the gene set variation analysis (GSVA) algorithm within the R package GSVA (Version 1.42.0).

Survival analysis

For each cancer type analyzed, TCGA transcriptomics and clinical data were obtained via the R package TCGAbiolinks (version 2.28.3),[87] then survival analysis was conducted by R package survival. Briefly, we performed gene set enrichment analysis using the ssGSEA algorithm in R package GSVA[54] to calculate enrichment scores for each cell type gene signatures. Then patients were split into mregDC^{high} and mregDC^{low} groups according to the median mregDC signature enrichment score. Furthermore, the *surv_cutpoint* function in R package survminer was utilized to determine the optimal cutting points for activated Treg signature enrichment scores in the mregDC^{high} group. Kaplan–Meier survival curve was modeled by *survfit* function. Hazard ratio (HR) and 95% CI in univariate and multivariate Cox proportional-hazards model were calculated by *coxph* function. The log-rank test was used to determine the statistical significance of differences between groups. (The marker genes for each cell type were listed in Table S2.).

QUANTIFICATION AND STATISTICAL ANALYSIS

Experimental group assignment was determined by genotype, and the experimental group is randomly assigned in the case of the same genotype. Data represent the mean ± standard deviation (SD) and mean ± standard error of the mean (SEM) calculated using GraphPad Prism 8 software. For pairwise comparisons, t-tests were used. For comparisons between more than two groups, one-way analysis of variance (ANOVA) was performed. All tests used are indicated in the figure legends. $P<0.05$ was considered to indicate statistical significance.